

Data efficient reinforcement learning and adaptive optimal perimeter control of network traffic dynamics

Can Chen ^a, Yunping Huang ^a, William H.K. Lam ^a, Tianlu Pan ^b, Shu-Chien Hsu ^a, Agachai Sumalee ^c, Renxin Zhong ^{d,*}

^aDepartment of Civil and Environmental Engineering, The Hong Kong Polytechnic University, Hong Kong.

^bResearch Institute for Smart Cities, School of Architecture and Urban Planning, Shenzhen University, China

^cSchool of Integrated Innovation, Chulalongkorn University, Bangkok, Thailand

^dSchool of Intelligent Systems Engineering, Sun Yat-Sen University, China.

Abstract

Existing data-driven and feedback traffic control strategies do not consider the heterogeneity of real-time data measurements. Besides, traditional reinforcement learning (RL) methods for traffic control usually converge slowly for lacking data efficiency. Moreover, conventional optimal perimeter control schemes require exact knowledge of the system dynamics and thus would be fragile to endogenous uncertainties. To handle these challenges, this work proposes an integral reinforcement learning (IRL) based approach to learning the macroscopic traffic dynamics for adaptive optimal perimeter control. This work makes the following primary contributions to the transportation literature: (a) A continuous-time control is developed with discrete gain updates to adapt to the discrete-time sensor data. Different from the conventional RL approaches, the reinforcement interval of the proposed IRL method can be varying with respect to the real-time resolution of data measurements. Approximate optimization methods are carried out to address the curse of dimensionality of the optimal control problem with consideration of the resolution of data measurement. (b) To reduce the sampling complexity and use the available data more efficiently, the experience replay (ER) technique is introduced to the IRL algorithm. (c) The proposed method relaxes the requirement on model calibration in a “model-free” manner that enables robustness against modeling uncertainty and enhances the real-time performance via a data-driven RL algorithm. (d) The convergence of the IRL-based algorithms and the stability of the controlled traffic dynamics are proven via the Lyapunov theory. The optimal control law is parameterized and then approximated by neural networks (NN), which moderates the computational complexity. Both state and input constraints are considered while no model linearization is required. Numerical examples and simulation experiments are presented to verify the effectiveness and efficiency of the proposed method.

Keywords: Macroscopic fundamental diagram, adaptive optimal perimeter control, heterogeneous data resolution, integral reinforcement learning, experience replay, closed-loop stability.

1. Introduction

Urbanization has induced dramatic growth in car usage in metropolises around the world, which results in growing traffic congestion, accidents and pollution. Efficient utilization of existing infrastructures via appropriate traffic control schemes is crucial to handling the fast-growing travel demand. Over the past decades, several traffic control strategies have been proposed and successfully implemented in practice (see [Papageorgiou et al., 2003](#), for an overview). Conventional traffic control methods such as SCOOT ([Hunt et al., 1982](#)), SCATS ([Lowrie, 1982](#)) and Traffic-responsive

*Corresponding author

E-mail addresses: can-caesar.chen@connect.polyu.hk (Can Chen), yunping.huang@connect.polyu.hk (Yunping Huang), william.lam@polyu.edu.hk (William H.K. Lam), luciatlpan@sina.cn (Tianlu Pan), mark.hsu@polyu.edu.hk (Shu-Chien Hsu), agachai.s@chula.ac.th (Agachai Sumalee), zhrenxin@mail.sysu.edu.cn (Renxin Zhong).

Urban Control (TUC) such as ALINEA (see Figure 12 in Papageorgiou et al., 2003), concentrate on link-level strategies. In the case of heterogeneous networks with multiple bottlenecks and heavily directional demand flows, local traffic-responsive metering controls such as TUC may not be optimal or might not achieve the stabilization of the system in a reasonable time period (Kouvelas et al., 2017). Oversaturated traffic conditions with queues spilling back to upstream links and the huge spatial dimension would introduce significant challenges to the local adaptive real-time traffic signal control strategies at the link level, i.e., SCOOT and SCATS (Gayah et al., 2014; Zhong et al., 2018a,b). Hence, under heavily saturated traffic conditions, traffic control strategies capturing network-level congestion should be devised to alleviate network congestion.

The network-level congestion can be significantly alleviated by identifying some critical intersections and regulating them effectively (Kouvelas et al., 2017). This finding gives rise to the concept of perimeter control by leveraging the recent advances in the macroscopic fundamental diagrams (MFDs). Pioneered by Godfrey (1969), with its existence proven by Daganzo (2007) theoretically, the MFDs have been widely investigated (Haddad and Geroliminis, 2012; Haddad et al., 2013; Keyvan-Ekbatani et al., 2013; Leclercq et al., 2014; Yildirimoglu and Geroliminis, 2014; Saeedmanesh and Geroliminis, 2017). The MFD intuitively describes a low-scatter relationship between the network vehicle accumulation and production, providing an analytically simple and computationally efficient framework for aggregate modeling of urban traffic network dynamics. Under the MFD framework, a heterogeneous urban traffic network is divided into several homogeneous regions with each admits a well-defined MFD (Ji and Geroliminis, 2012). Under certain regularity conditions, such as stationary (or slow-varying) and evenly distributed demand, well-defined MFDs were evidenced by both simulation-based experiments (Gartner and Wagner, 2004) and empirical investigations (Geroliminis and Daganzo, 2008). In particular, Loder et al. (2019) empirically observed the existence of the MFDs and their critical point variations using billions of vehicle observations from more than 40 cities. Further analytical consideration and empirical evidence have been provided by Daganzo and Geroliminis (2008); Helbing (2009); Ji et al. (2010); Gayah and Daganzo (2011); Daganzo et al. (2011). However, heterogeneous networks, in essence, do not exhibit a well-defined MFD. Such a network can be modeled by a set of differential equations governing the traffic flow conservation in conjunction with MFDs as long as it can be partitioned into homogeneous subregions with each admits a well-defined MFD (Ji and Geroliminis, 2012).

Considerable research efforts have been dedicated to devising optimal network traffic control strategies based on MFDs. The perimeter control is believed to be a promising solution to address spatial dimension challenge while considering the network-scale traffic congestion. Recent studies showed that feedback-based gating/perimeter control is efficient in mitigating congestion in the protected urban networks by exploiting MFDs. One goal is to manipulate the regional accumulation to the desired equilibrium (e.g., to operate the protected regions around the critical accumulation that maximizes flow), i.e., set-point control. Aboudolas and Geroliminis (2013) used linear-quadratic-integral (LQI) and linear-quadratic-regulator (LQR) to operate the MFD system to approach the equilibrium points while Keyvan-Ekbatani et al. (2012) utilized a proportional-integral (PI) controller considering system uncertainty. Keyvan-Ekbatani et al. (2013, 2015a,b) solved the set-point control problem using the PI controller with consideration of boundary queue in MFDs, and different kinds of uncertainty and disturbance were included in the simulations. Haddad and Mirkin (2016) proposed a transfer function embedded with time delay to deal with the set-point control problem. Another goal is to achieve the maximum trip completion flow or to minimize the total travel time of the road network by properly restricting the inflow traffic to the network. Daganzo (2007) applied the MFD framework to devise a control rule that maximizes the network trip completion rate. Geroliminis et al. (2013); Ramezani et al. (2015) solved the optimal perimeter control problem within standard two-region MFD system by model predictive control (MPC) while Haddad et al. (2013) implemented MPC on a mixed network. Other optimal perimeter controls of the MFD system using MPC were in a hierarchical scheme (Zhou et al., 2016; Fu et al., 2017). Aalipour et al. (2018) derived an analytical optimal control policy by solving the Hamilton-Jacobi-Bellman (HJB) equation for maximizing the trip completion rates. Apart from optimal control using the MFD framework, the robust perimeter control problem of the MFD-based network traffic was also addressed in previous studies using linear matrix inequalities, e.g., Haddad and Shraiber (2014); Haddad (2015). All the above methods require linearization of the MFD function except for Zhong et al. (2018a); Sirmatel and Geroliminis (2021). Sirmatel and Geroliminis (2019) developed a nonlinear moving horizon estimation scheme for large-scale urban networks subject to measurement noises in state and inflow demand. Li et al. (2021) proposed a sliding mode controller for two-region MFD based networks considering cordon queues and heterogeneous transfer flows. Other recent efforts were put to devising resilient perimeter control under cyberattacks (Mercader and Haddad, 2021), real-time state estimation in multi-region MFD urban networks (Saeed-

manesh et al., 2021), multi-region extension for the M-model that captures the effects of remaining travel distance dynamics (Sirmatel et al., 2021), perimeter control for congested areas against state degradation risk (Ding et al., 2020), optimal perimeter control considering coupled/decoupled controllers (Haddad, 2017a) and aggregate boundary queue dynamics (Haddad, 2017b).

The aforementioned studies on perimeter control can be regarded as model-based traffic responsive control. Specifically, previous studies on the feedback-based perimeter control were derived under one common assumption that the model parameters can be accurately calibrated. For optimal perimeter control, in particular, it is generally assumed that perfect knowledge of the network is available and the parameters will not change during the planning horizon. Moreover, local linearization around the desired equilibrium is widely performed to simplify the control design. Apart from model-based traffic responsive control, considerable research efforts have focused on adaptive perimeter control which must adapt to a controlled system with time-varying and/or uncertain parameters or external disturbances such as travel demand noise. By considering the boundary queue that can have a negative impact on upstream queue modeling, Kouvelas et al. (2017) introduced an online adaptive parameters optimization algorithm for perimeter control. Haddad and Zheng (2020) designed the distributed adaptive perimeter control laws with control gains varying with time considering state delays and interconnection delays. Since traffic networks are subject to various uncertainties, parameters of MFDs are uncertain and time-varying. Also, the travel demand and traffic control strategies can significantly affect the shape of the MFD (Geroliminis and Boyacı, 2012). The performance of these control strategies increasingly deteriorates with increasing disturbance prediction and model errors (Zhong et al., 2014; Baldi et al., 2019). Nevertheless, as specified in Kouvelas et al. (2017), in many cases the adopted models are calibrated once and would not be re-calibrated regularly. This causes a defect in their field experiments. Despite the vast literature related to modeling and control with MFDs, the design of dynamic control policies to various exogenous disturbances that can affect the dynamics is seldom considered. To adapt the real-time observation and then the control to operate the traffic network optimally, it is necessary to keep adjusting the model parameters (Kouvelas et al., 2017). However, this process can be a heavy computational burden and difficult to be implemented in real-time (Modares et al., 2014). For an ever-changing traffic environment subject to various exogenous disturbances, a predefined model-based traffic responsive policy may become suboptimal or even impractical. Yet in the literature, to the best knowledge of the authors, few existing studies dealt with the problem of devising the adaptive control strategies for MFD systems with (partially) unknown system dynamics. Lei et al. (2019) and Ren et al. (2020) devised a “model-free” perimeter controller for a multi-region MFD-based network via the iterative learning control by assuming recurrent traffic conditions that the traffic dynamics would not admit a significant change in a day-to-day time-scale during the learning period.

The emerging big data technology gives rise to data-driven approaches to solving the aforementioned difficulties. Rooted in computer science, the reinforcement learning (RL) has attracted increasing attention recently for its success in video games (Mnih et al., 2015) and Go (Silver et al., 2016). Under the RL setting, an agent optimizes a goal-oriented long-term reward via policy learning. At each step, the RL agent interacts with the environment and evaluates the performance of its action based on the feedback from the environment. The agent then tries to improve the performance of subsequent actions (Sutton and Barto, 2018). A reformulation of RL is called adaptive dynamic programming (ADP) in economics and management communities. The RL and ADP bridge the gap between optimal control and adaptive control. In an off-line manner, the RL and ADP provide an approximate solution to the optimal control problem obtained from the Pontryagin’s minimum principle and the dynamic programming principle (i.e., the HJB equation). Solving the HJB equation takes the center stage in deriving optimal control strategies. However, the HJB equation is generally intractable to be solved by analytical approaches for strong nonlinearity, possible discontinuities in the solution and the curse of dimensionality. To handle the curse of dimensionality in optimal traffic signal control design for large-scale networks, Baldi et al. (2019) parametrized the solution of the HJB equation using an appropriate Lyapunov function. The simulation results showed that the approximately optimal traffic signal control design via low-complexity parametrization of the HJB equation can provide a satisfactory trade-off between computational complexity and network performance. However, there is a lack of analytical proof of the convergence as well as the explicit consideration of saturated constraints on the system state and input in Baldi et al. (2019). A conventional ADP based RL algorithm was proposed by Su et al. (2020) to provide an analytical optimal perimeter control law for the MFD dynamics. Both convergence and stability of the closed-loop system were achieved. However, conventional approximation techniques for solving the HJB equations require complete or partial knowledge of the system dynamics and are normally off-line. Thus, they cannot handle modeling uncertainties and be deployed for real-time

applications.

The RL and ADP help the optimal control circumvent the requirement on complete knowledge of the system dynamics so that uncertainties and changes in dynamics can be incorporated into the optimal control framework. Compared with the off-line nature of the conventional optimal control framework, the RL and ADP can find the optimal solution online in real-time using data-driven mechanism meanwhile robustness and adaptiveness can be well achieved. Data-driven deep reinforcement learning has been incorporated in solving traffic optimization problems (Kheterpal et al., 2018). RL in the data-driven control community gives rise to a promising solution for optimal perimeter control problems in a “model-free” manner. Zhou and Gayah (2021) proposed a deep RL based scheme for the two-region perimeter control problems, which can achieve comparable performances to the MPC approach.

Considering that traffic data are collected from sensors in a discrete-time manner, we would like to establish a continuous-time control (MFD dynamics) with discrete gain updates (adapting to the sensor data). Generally, the sample time interval of the data collected by a type of sensor is fixed. Thus, sensors of various types deployed in a traffic network would be heterogeneous with different resolutions of data measurements. It would be much better if the reinforcement intervals can be varying with respect to the real-time resolutions of data measurements, i.e., the reinforcement intervals can be selected online to ensure the data-driven RL algorithms do have rich data. Existing works utilizing RL such as Su et al. (2020); Zhou and Gayah (2021) do not consider such issues. Different from the traditional online RL approaches, the reinforcement intervals of the integral reinforcement learning (IRL) need not be identical and can be adjusted online, which consequently is more suitable for real-world traffic data measurement and allows adaptive online learning to guarantee real-time performance. Based on the idea of IRL, an equivalent Bellman equation, namely the IRL Bellman equation was developed. An online policy iteration algorithm was developed for the optimal control problem of continuous-time systems via solving the IRL Bellman equation in Vrabie et al. (2009). This adaptive optimal control does not explicitly employ the knowledge on system dynamics, i.e., “model-free”.

The actor-critic (AC) structure contributes significantly to the success of RL algorithms. In the AC structure, the actor deploys a control policy to the system or environment, while the critic evaluates the cost induced by the implemented control policy and provides reward signals to the actor. The actor-critic dual neural networks (AC-NN) can be used to circumvent the “curse of dimensionality”. Despite the adaptive learning capability, traditional RL approaches usually converge slowly for lacking data efficiency, which is a major obstacle to real-time applications. Experience replay (ER) technique, also known as concurrent learning, provides a promising approach to improve the efficiency of RL algorithms¹. The ER technique uses historical and current data simultaneously in a “smart” manner. It has been found that the AC structure can be integrated with the ER technique to improve the data efficiency and convergent speed of RL algorithms (Modares et al., 2014).

To handle the aforementioned challenges, this paper makes the following primary contributions to the transportation literature.

- Robustness to heterogeneous data resolutions. Unlike the conventional RL algorithms, the reinforcement intervals of the proposed IRL approach can be selected online to adapt to heterogeneous real-time data resolutions. The introduction of the ER technique to RL algorithms can speed up their convergence when limited real-time data are available due to unexpected longer sample time intervals.
- Data efficiency. In the ER technique, a number of recent samples are stored in a database and are presented repeatedly to the underlying RL algorithm, which enhances their data efficiency. An easy-check rank condition is introduced to verify the data richness requirement and reduce sampling complexity.
- Model-free against modeling uncertainties. It is desirable for the controller to handle the modeling uncertainties. Unlike the previous studies which rely on exact knowledge of the underlying system dynamics, a key advantage of the proposed method is that the exact knowledge of the traffic model is no longer needed. Also, the proposed approach does not rely on the widely used model linearization.
- Incorporating real-time data-driven components for adaptiveness. It is necessary to enable the controller to adapt to the real-time traffic conditions, e.g., traffic incidents. To this end, an online adaptive data-driven perimeter controller is devised.
- Convergence and stability guaranteed. Unlike many existing studies in the transportation literature that use RL algorithms without proof of convergence nor stability, this work guarantees the closed-loop stability of

¹ Another benefit of ER is conquering the difficulty arising in the persistently exciting condition for nonlinear systems.

the overall system by leveraging the RL with Lyapunov theory. The input and state constraints are explicitly considered in the proposed IRL algorithms.

This paper is organized as follows: [Section 2](#) provides a brief introduction to dynamic programming and IRL. [Section 3](#) discusses the optimal perimeter control problem formulation. [Section 4](#) develops a model-free data-driven IRL method for optimal adaptive perimeter control. Then [Section 5](#) performs the implementations of the proposed on-line iterative learning algorithm with NNs. Numerical results are presented in [Section 6](#) and a microscopic simulation experiment is provided in [Section 7](#). Finally, [Section 8](#) provides concluding remarks. For convenience, we summarize the key notation used in this paper in [Table 1](#).

Table 1: List of key notations

Symbol	Meaning
\mathbb{R}	The set of all real numbers
\mathbb{R}^m	The Euclidean space of all real m -vectors
$\mathbb{R}^{n \times m}$	The space of all $n \times m$ real matrices
T	The transposition symbol
Ω	A compact set of \mathbb{R}^n
$C^m(\Omega)$	The class of functions having continuous m -th derivative on Ω
$\ x(t)\ _{L_2}$	The L_2 norm of continuous-time function $x(t)$ while we use $\ x(t)\ $ for brevity
$>$	A matrix $R > 0$ means that it is positive definite and \geq denotes positive semi-definite
\otimes	Kronecker product: $\forall A \in \mathbb{R}^{m \times n}, B \in \mathbb{R}^{p \times q}, A \otimes B \triangleq \begin{bmatrix} a_{11}B & \cdots & a_{1n}B \\ \vdots & \ddots & \vdots \\ a_{m1}B & \cdots & a_{mn}B \end{bmatrix}$
\odot	Hadamard product: $\forall A, B \in \mathbb{R}^{m \times n}, A \odot B \triangleq \begin{bmatrix} a_{11}b_{11} & \cdots & a_{1n}b_{1n} \\ \vdots & \ddots & \vdots \\ a_{m1}b_{m1} & \cdots & a_{mn}b_{mn} \end{bmatrix}$
Z_i	The directly reachable regions from region i except itself, i.e., $i \notin Z_i$
$n_{ij}(t)$	Number of vehicles in region i with destination to region j at time t
$n_i(t)$	Accumulation or total number of vehicles in region i at time t , and $n_i(t) = n_{ii}(t) + \sum_{j \in Z_i} n_{ij}(t)$
$q_{ij}(t)$	Travel demand defined as a flow in which its origin is region i and destination is region j
$u_{ij}(t)$	Perimeter controllers controlling the ratio of the transfer flow that transfers from region i to region j at time t
$G_i(n_i(t))$	MFD that maps the network accumulation $n_i(t)$ to trip completion rate for region i at time t
α_n	The dimension of the accumulation state n
α_u	the dimension of the perimeter control u
α_q	the dimension of the travel demand q

For a better grasp of the logical structure of this paper, the flow for reasoning is depicted in [Figure 1](#). Consider the MFD based system in the affine form as (14). In the optimal regulation problem, the objective is to design an optimal perimeter control such that the accumulation state converges to the desired equilibrium by minimizing a cost functional defined by (15). This optimal cost function and perimeter control can be derived via solving an equivalent HJB equation (21). Note that the solution of (21) may be intractable due to its strong nonlinearity. One of the most common methods to resolve this difficulty is the policy iteration method (25)-(26). However, because of the heterogeneity of real-time data measurements and the lack of complete knowledge on the system dynamics, we cannot apply the policy iteration method directly in practice. Hence, an equivalent formulation of the policy iteration method, namely, the IRL Bellman equation given by (32) is established, which can adapt to the time-varying real-time data resolution and does not involve the system dynamics, i.e., “model-free”. Finally, based on (32), an online iterative learning scheme with experience replay adaptation law (43) are established, which can be implemented with the AC-NN framework (40) to boost the computational efficiency and approximate the optimal perimeter controller \tilde{u}^* .

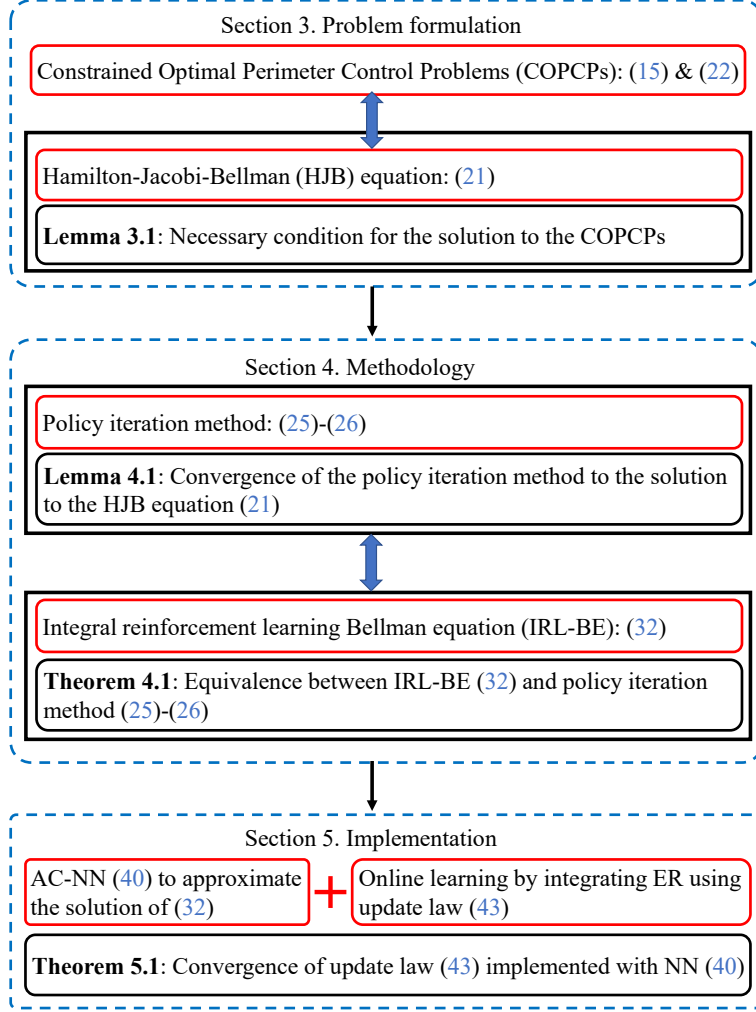


Figure 1: Gallery of this study

2. Preliminaries: dynamic programming and integral reinforcement learning

In this section, we outline how the HJB equation couples the performance functional, the nonlinear system dynamics, the IRL Bellman equation, and the neural network framework.

Consider the nonlinear system in the affine form as

$$\begin{aligned} \dot{x}(t) &= f(x(t)) + g(x(t))u(t) \\ y(t) &= l(x(t)) \end{aligned} \tag{1}$$

where $x(t) \in \mathbb{R}^n$, $u(t) \in \mathbb{R}^m$, and $y(t) \in \mathbb{R}^p$ represent the state, the control input, and the output of (1), respectively. We call $f(x(t)) \in \mathbb{R}^n$ the drift dynamics, $g(x(t)) \in \mathbb{R}^{n \times m}$ the input dynamics, and $l(x(t)) \in \mathbb{R}^p$ the output dynamics, respectively. It is assumed that $f(0) = 0$ and $f(x(t)) + g(x(t))u(t)$ is locally Lipschitz and the system is stabilizable.

In the optimal regulation problem, the objective is to design an optimal control input such that the controlled state of (1) converges to the desired equilibrium by minimizing a cost functional defined as

$$J(x(0), u) = \int_0^\infty \mathcal{L}(x(t), u(t)) dt \equiv \int_0^\infty (N(x(t)) + U(u(t))) dt$$

where $N(x) \geq 0$ and $U(u) \geq 0$, with \geq denotes positive semi-definite. Generally, we choose $U(u) = u^T R u$, $R = R^T > 0$ and $R \in \mathbb{R}^{m \times m}$ for unconstrained control case with $>$ denotes positive definite. However, for many real applications, u is saturated, i.e., $|u_\xi| \leq \lambda$, $\xi = 1, \dots, m$, where $\lambda > 0$ is the performance limit of the actuator. Abu-Khalaf et al. (2008) proposed the following generalized non-quadratic functional to consider the effect of saturation on control input u .

$$U(u) = 2 \int_0^u \lambda \tanh^{-T}(s/\lambda) R ds, \quad \lambda > 0$$

Without loss of generality, let $R = \text{diag}(\gamma_1, \dots, \gamma_m)$ be a positive definite matrix of proper dimension.

Definition 2.1. (Admissible Control) A control policy μ is admissible to (1), if $\mu(x)$ is continuous on Ω , $\mu(0) = 0$ and μ stabilizes the system (1) on Ω with the value function (2) being finite for $\forall x_0 \in \Omega$. ■

The value function for an admissible control policy can be defined as

$$V(x, u) = \int_t^\infty \mathcal{L}(x(\tau), u(\tau)) d\tau \equiv \int_t^\infty (N(x(\tau)) + U(u(\tau))) d\tau \quad (2)$$

The Hamiltonian function is

$$H\left(x, u, \frac{\partial V}{\partial x}\right) = \mathcal{L}(x, u) + \left(\frac{\partial V}{\partial x}\right)^T (f(x) + g(x)u)$$

Since the integrand of the performance functional does not depend on time explicitly and the terminal time is fixed (or infinite time) while (1) is an autonomous dynamical system, the optimality is given by $H\left(x, u, \frac{\partial V}{\partial x}\right) = 0$, i.e., the Bellman optimality equation

$$\mathcal{L}(x, u^*) + \left(\frac{\partial V^*}{\partial x}\right)^T (f(x) + g(x)u^*) = 0 \quad (3)$$

The optimal control can be obtained as

$$u^* = -\lambda \tanh\left(\frac{1}{2\lambda} R^{-1} g^T(x) \frac{\partial V^*}{\partial x}\right) \quad (4)$$

Since sensors collect data and transfer them to the controllers with prescribed time resolutions, we cannot apply the Bellman equation (3) directly in practice. Moreover, (3) involves the exact system dynamics $f(x)$ and $g(x)$. To relax this requirement and to consider sensor data measurements, an equivalent formulation of the the Bellman equation (3) that does not involve the drift dynamics can be established

$$V(x(t)) = \int_t^{t+\Delta t} (N(x(\tau)) + U(u(\tau))) d\tau + V(x(t + \Delta t))$$

for any time $t \geq 0$ and time interval $\Delta t > 0$. Δt is termed as the reinforcement interval, which can be adjusted in real-time according to the resolution of sensor data and the learning rate of the RL based algorithms. This equation is called IRL Bellman equation. By iterating on the IRL Bellman equation and updating the control policy, we can obtain both the value function and the optimal control.

Given an admissible policy u_0 , for $j = 0, 1, \dots$, given u_j , solve for the value $V_{j+1}(x)$ using the following IRL Bellman equation in iteration.

$$V_{j+1}(x(t)) = \int_t^{t+\Delta t} (N(x(\tau)) + U(u_j(\tau))) d\tau + V_{j+1}(x(t + \Delta t)) \quad (5)$$

on convergence, set $V_{j+1}(x(t)) = V_j(x(t))$. Update the control policy $u_{j+1}(x(t))$ using

$$u_{j+1}(x(t)) = -\lambda \tanh\left(\frac{1}{2\lambda} R^{-1} g^T(x(t)) \frac{\partial V_{j+1}}{\partial x}\right) \quad (6)$$

(5)-(6) are known as an on-policy RL algorithm².

To uniformly approximate the value function in (5), we can use the following neural-network-type structure.

$$\hat{V}(x) = \hat{W}_c^T \phi_1(x)$$

where $\phi_1(x) : \mathbb{R}^n \rightarrow \mathbb{R}^N$ is the basis function vector and N is the number of basis functions. With this value function approximation, its partial derivative $\frac{\partial \hat{V}}{\partial x}$ can be approximated accordingly. Using the above approximated value function, the constrained optimal control in (4) can be generated by

$$\hat{u} = -\lambda \tanh \left(\frac{1}{2\lambda} R^{-1} g^T(x) \hat{W}_c^T \frac{\partial \phi_1}{\partial x} \right)$$

Incorporating these approximations into the IRL Bellman equation yields

$$e(t) = \Delta \phi_1(x(t))^T \hat{W}_c + \int_{t-\Delta t}^t (N(x(\tau)) + U(\hat{u}(\tau))) d\tau$$

where $\Delta \phi_1(x(t)) = \phi_1(x(t)) - \phi_1(x(t-\Delta t))$ and e is the temporal difference (TD) error after using current approximated critic weight \hat{W}_c . To avoid the case that there are insufficient real-time data for updating the weights of the learning network and to use the data in the history stack efficiently, we consider $\Delta \phi_1(x(t_j))$ as evaluated values of $\Delta \phi_1$ at the recorded time t_j . Then, we define the Bellman equation error (i.e., TD error) at the recorded time t_j using the current critic weight estimation \hat{W}_c as

$$e(t_j) = \Delta \phi_1(t_j)^T \hat{W}_c + \int_{t_j-\Delta t}^{t_j} (N(x(\tau)) + U(\hat{u}(\tau))) d\tau$$

Recent transition samples (historical data) are stored and repeatedly presented to the gradient-based update rule of the weights of the learning network (7) so as to speed up the computation and to obtain an easy-to-check convergent condition for the IRL algorithm. This process is known as the experience replay (ER) technique. The weights of the learning network are updated via minimizing simultaneously the instantaneous TD error (the first part of (7) from real-time measurement) and the TD errors for the stored transition samples (the second part of (7)), which is given as

$$\dot{\hat{W}}_c = -\alpha_c \frac{\Delta \phi_1(x(t))}{(\Delta \phi_1(x(t))^T \Delta \phi_1(x(t)) + 1)^2} e(t) - \alpha_c \sum_{j=1}^l \frac{\Delta \phi_1(x(t_j))}{(\Delta \phi_1(x(t_j))^T \Delta \phi_1(x(t_j)) + 1)^2} e(t_j) \quad (7)$$

The optimal policy (6) implemented by the on-policy IRL algorithms does not require the knowledge of $f(x)$. However, it still relies on the input dynamics $g(x)$. To get rid of $g(x)$, we may adopt an off-policy IRL algorithm that the control implemented (nearly optimal) can be different from the optimal control (6). Towards this, we rewrite the affine dynamics as

$$\dot{x}(t) = f(x(t)) + g(x(t))u_j(t) + g(x(t))(u(t) - u_j(t)) \quad (8)$$

where $u_j(t)$ is the policy to be updated and $u(t)$ is the behavior policy that is actually implemented to the system dynamics to generate the data for learning. Differentiating the value function $V(x)$ along the system trajectory (8) and using (6) yields

$$\dot{V}_j = \left(\frac{\partial V_j(x)}{\partial x} \right)^T (f + g u_j) + \left(\frac{\partial V_j(x)}{\partial x} \right)^T g (u_{j+1} - u_j) = -N(x) - 2\varrho^T(u_{j+1})R(u_{j+1} - u_j) - 2 \int_0^{u_j} \varrho^T(s)R ds$$

²On-policy and off-policy RL algorithms are devised in the literature. Their essential difference lies in how the target policy and the behavior policy are implemented. The target policy is what we are learning about, i.e., the optimal control law or the solution to the HJB equation. The target policy can be regarded as the ideal optimal policy. The behavior policy generates the action and behavior, which can be regarded as the policy implemented. The target policy and the behavior policy are the same for on-policy RL algorithms while they are different for off-policy algorithms. Generally, similar to the decision process of human beings, the off-policy algorithms can learn the optimal policies but implement suboptimal policies.

where $\varrho(s) = \lambda \tanh^{-1}(s/\lambda)$. Integrating the above equation yields the off-policy IRL Bellman equation

$$V_j(x(t + \Delta t)) - V_j(x(t)) = \int_t^{t+\Delta t} \left(-N(x) - 2\varrho^T(u_{j+1})R(u_{j+1} - u_j) - 2 \int_0^{u_j} \varrho^T(s)Rds \right) d\tau \quad (9)$$

For an implemented control policy $u(t)$, the off-policy IRL Bellman equation (9) can be solved for both value function V_j and updated policy u_{j+1} simultaneously without requiring any knowledge about the system dynamics.

3. Problem statement

In this section, we first recapitulate the dynamics for a traffic network modeled by multi-region MFD systems. We then discuss the optimal perimeter control problem formulation.

3.1. The multi-region MFD framework

A heterogeneous urban network decomposed into L ($L > 1$) homogeneous subregions wherein each region admits a well-defined MFD is considered in line with Haddad (2015); Zhong et al. (2018b). Let the state vector be $n(t) \triangleq [n_{11}(t), \dots, n_{ij}(t), \dots, n_{LL}(t)]^T \in \mathbb{R}^{\alpha_n}$ and the travel demand vector be $q(t) \triangleq [q_{11}(t), \dots, q_{ij}(t), \dots, q_{LL}(t)]^T \in \mathbb{R}^{\alpha_q}$, respectively. The control vector is $u(t) \triangleq [u_{12}(t), \dots, u_{ij}(t), \dots, u_{Lj}(t)]^T \in \mathbb{R}^{\alpha_u}$, where $u_{ij}(t)$ controls the ratio of the transfer flow that transfer from region i to j at time t . Note that $n_i(t)$ and $u_{ij}(t)$ are subject to heterogeneous constraints as given by (11a)-(11b). The dynamic flow conservation equations of the multi-region MFD system are then formulated as follows:

$$\frac{dn_{ii}(t)}{dt} = -\frac{n_{ii}(t)}{n_i(t)}G_i(n_i(t)) + \sum_{j \in Z_i} \frac{n_{ji}(t)}{n_j(t)}G_j(n_j(t))u_{ji}(t) + q_{ii}(t) \quad (10a)$$

$$\frac{dn_{ij}(t)}{dt} = -\frac{n_{ij}(t)}{n_i(t)}G_i(n_i(t))u_{ij}(t) + q_{ij}(t) \quad (10b)$$

$$n_i(t) = n_{ii}(t) + \sum_{j \in Z_i} n_{ij}(t) \quad (10c)$$

subject to

$$0 \leq n_i(t) \leq n_i^{jam} \quad (11a)$$

$$0 \leq u_{ij}^{\min} \leq u_{ij}(t) \leq u_{ij}^{\max} \leq 1 \quad (11b)$$

where $i = 1, \dots, L$ and $j \neq i$. The state dynamics (10a)-(10b) can be written in the following affine form (Su et al., 2020):

$$\dot{n}(t) = F(n(t)) + S(n(t))u(t) \quad (12)$$

One significant traffic management purpose is to devise perimeter control $u(t)$ to regulate the cross-boundary flows such that the network accumulations $n(t)$ can converge to the desired equilibrium n^* , i.e., set-point control (Zhong et al., 2018a,b). The steady state n^* and the corresponding control input u^* can be solved from the steady-state equations (Haddad and Shraiber, 2014; Zhong et al., 2018b):

$$\frac{dn_{ii}^*}{dt} = 0 = -\frac{n_{ii}^*}{\bar{n}_i}G_i(\bar{n}_i) + \sum_{j \in Z_i} \frac{n_{ji}^*}{\bar{n}_j}G_j(\bar{n}_j)u_{ji}^* + q_{ii}^* \quad (13a)$$

$$\frac{dn_{ij}^*}{dt} = 0 = -\frac{n_{ij}^*}{\bar{n}_i}G_i(\bar{n}_i)u_{ij}^* + q_{ij}^* \quad (13b)$$

$$\bar{n}_i = n_{ii}^* + \sum_{j \in Z_i} n_{ij}^* \quad (13c)$$

subject to

$$0 \leq \bar{n}_i \leq n_i^{jam}, \quad 0 \leq u_{ij}^{\min} \leq u_{ij}^* \leq u_{ij}^{\max} \leq 1$$

where q_{ii}^* and q_{ij}^* are nominal demand patterns.

It is a common practice to perform a coordinate transformation to reformulate the set-point control problem into a stabilization problem (Zhong et al., 2018a,b). We define $\tilde{n}(t) = [\tilde{n}_1(t), \dots, \tilde{n}_{\alpha_n}(t)]^T \in \mathbb{R}^{\alpha_n}$ and $\tilde{u}(t) = [\tilde{u}_1(t), \dots, \tilde{u}_{\alpha_u}(t)]^T \in \mathbb{R}^{\alpha_u}$ as the new state vector and new control vector, respectively. $\tilde{n} = n - n^*$ denotes the difference between the actual accumulation and the desired steady-state accumulation, while $\tilde{u} = u - u^*$ is the difference between the actual control input and the steady-state control input. After the coordinate transformation, the multi-region MFD system (10a)-(10c) can be expressed by the following standard affine form:

$$\dot{\tilde{n}}(t) = \mathbf{F}(\tilde{n}(t)) + \mathbf{S}(\tilde{n}(t))\tilde{u}(t) \quad (14)$$

Both the state vector and the control vector of system (14) are restricted into some compact sets say $\tilde{n}(t) \in \Omega \subset \mathbb{R}^{\alpha_n}$ and $\tilde{u}(t) \in \mathcal{U} \subset \mathbb{R}^{\alpha_u}$, where Ω and \mathcal{U} are the universal sets of \tilde{n} and \tilde{u} , respectively. \mathbf{F} and \mathbf{S} are unknown Lipschitz continuous nonlinear functions on $\Omega \subset \mathbb{R}^{\alpha_n}$ containing the origin.

In Appendix A, we present the dynamics in the affine form for the two-region and the three-region MFD systems, which are widely investigated in the literature.

3.2. Optimal perimeter control of multi-region MFD system

Set-point control and minimizing the total time spent (TTS) are two main objectives considered in the optimal perimeter control problem of MFD systems. In this subsection, we present the formulation of constrained optimal perimeter control problem (COPCP) for multi-region MFD systems considering heterogeneous cross-boundary capacities.

As a special case, Su et al. (2020) showed that the set-point control problem of the two-region MFD system could be modeled as a constrained optimal control problem. We will extend the formulation of set-point constrained optimal perimeter control problem (S-COPCP) for the two-region MFD system to general multi-region MFD systems while considering the heterogeneous cross-boundary capacities. We will also derive the necessary condition for the S-COPCP of multi-region MFD systems. Next, we will present the COPCP for minimizing TTS (T-COPCP) of the multi-region MFD system and derive the optimal perimeter control law for the T-COPCP.

Set-point COPCP (S-COPCP) of the Multi-region MFD System

Consider the multi-region MFD system (14), find the perimeter controller \tilde{u} to minimize the following objective function:

$$\min_{\tilde{u}} J(\tilde{n}_0) = \int_0^\infty \mathcal{L}(\tilde{n}(t), \tilde{u}(t)) dt \quad (15)$$

subject to (14)

where $\tilde{n} \in \Omega \subset \mathbb{R}^{\alpha_n}$ and $\tilde{u} \in \mathcal{U} \subset \mathbb{R}^{\alpha_u}$.

The utility function for the S-COPCP is given by

$$\mathcal{L}(\tilde{n}(t), \tilde{u}(t)) \triangleq N(\tilde{n}(t)) + U(\tilde{u}(t)) \quad (16)$$

where $N(\tilde{n})$ represents the cumulative error between the system state and the desired equilibrium, and $U(\tilde{u})$ is the required control effort for unconstrained control case. Generally, $N(\tilde{n}) \triangleq \tilde{n}^T Q \tilde{n} \geq 0$ with $Q \in \mathbb{R}^{\alpha_n \times \alpha_n}$ and $Q > 0$, and $U(\tilde{u}) \triangleq \tilde{u}^T R \tilde{u} \geq 0$ with $R \in \mathbb{R}^{\alpha_u \times \alpha_u}$ and $R > 0$.

Without loss of generality, let $R = \text{diag}(\gamma_1, \dots, \gamma_{\alpha_u}) \in \mathbb{R}^{\alpha_u \times \alpha_u}$ with $\gamma_{k_u} > 0$, $k_u = 1, \dots, \alpha_u$. To handle the heterogeneous cross-boundary capacities (11b) in the perimeter controller design, i.e., $\tilde{u}_{k_u}^{\min} \leq \tilde{u}_{k_u} \leq \tilde{u}_{k_u}^{\max}$, inspired by Abu-Khalaf et al. (2006) and Lyshevski (1998), for each \tilde{u}_{k_u} we define the following function:

$$U_{k_u}(\tilde{u}_{k_u}) = 2\gamma_{k_u} \int_{\tilde{v}_{k_u}}^{\tilde{u}_{k_u}} \tanh^{-1} \left(\frac{v_{k_u} - \bar{v}_{k_u}}{\gamma_{k_u}} \right) dv_{k_u}$$

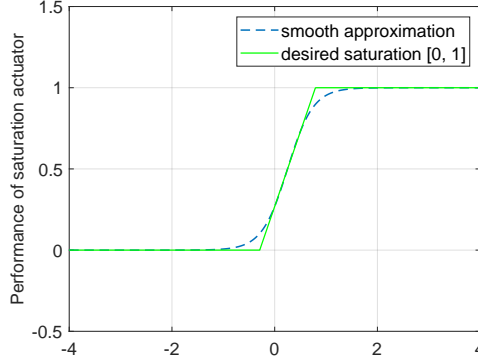


Figure 2: Performance of the proposed saturation actuator

where $\bar{v}_{k_u} = \frac{\tilde{u}_{k_u}^{\max} + \tilde{u}_{k_u}^{\min}}{2}$, $\underline{v}_{k_u} = \frac{\tilde{u}_{k_u}^{\max} - \tilde{u}_{k_u}^{\min}}{2}$. Based on the features of inverse hyperbolic tangent function, $U_{k_u}(\tilde{u}_{k_u})$ can be regarded as a penalty function which limits the input \tilde{u}_{k_u} to $(\tilde{u}_{k_u}^{\min}, \tilde{u}_{k_u}^{\max})$. Figure 2 shows that the saturation actuator (blue dotted line) developed by the proposed penalty function can well approximate the non-smooth control constraint (green solid line) in a smooth manner. Thus, $U(\tilde{u})$ is defined as

$$U(\tilde{u}) = \sum_{k_u=1}^{\alpha_u} U_{k_u}(\tilde{u}_{k_u}) = \sum_{k_u=1}^{\alpha_u} 2\underline{v}_{k_u} \gamma_{k_u} \int_{\bar{v}_{k_u}}^{\tilde{u}_{k_u}} \tanh^{-1}\left(\frac{v_{k_u} - \bar{v}_{k_u}}{\underline{v}_{k_u}}\right) dv_{k_u} = 2\underline{v}^T R \int_{\bar{v}}^{\tilde{u}} \tanh^{-1}\left(\frac{1}{\underline{v}} \odot (v - \bar{v})\right) dv \quad (17)$$

where $\bar{v} \triangleq [\bar{v}_1, \dots, \bar{v}_{\alpha_u}]^T \in \mathbb{R}^{\alpha_u}$, $\underline{v} \triangleq [\underline{v}_1, \dots, \underline{v}_{\alpha_u}]^T \in \mathbb{R}^{\alpha_u}$.

The value function $V: \mathbb{R}^{\alpha_n} \rightarrow \mathbb{R}$ is defined as

$$V(\tilde{n}(t)) = \int_t^\infty \mathcal{L}(\tilde{n}(\tau), \tilde{u}(\tau)) d\tau \equiv \int_t^\infty (N(\tilde{n}(\tau)) + U(\tilde{u}(\tau))) d\tau = \int_t^\infty \left(\tilde{n}^T(\tau) Q \tilde{n}(\tau) + 2\underline{v}^T R \int_{\bar{v}}^{\tilde{u}(\tau)} \tanh^{-1}\left(\frac{1}{\underline{v}} \odot (v - \bar{v})\right) dv \right) d\tau \quad (18)$$

Following the development in Section 2, we can obtain the following Bellman equation

$$\mathcal{L}(\tilde{n}(t), \tilde{u}(t)) + \left(\frac{\partial V}{\partial \tilde{n}}\right)^T (\mathbf{F}(\tilde{n}) + \mathbf{S}(\tilde{n})\tilde{u}) = 0 \quad (19)$$

Now we can present the necessary condition for the solution to the S-COPCP of the multi-region MFD system.

Lemma 3.1. Suppose that V^* is the optimal value function for the S-COPCP of the multi-region MFD system. It follows that

- 1) the constrained optimal perimeter control is given by

$$\tilde{u}^* = -\underline{v} \odot \tanh(D^*) + \bar{v}, \text{ with } D^* = \frac{1}{2\underline{v}} \odot \left(R^{-1} \mathbf{S}^T \frac{\partial V^*}{\partial \tilde{n}} \right) \quad (20)$$

where $D^* = [D_1^*, \dots, D_{\alpha_u}^*]^T \in \mathbb{R}^{\alpha_u}$ is the unconstrained optimal control input;

- 2) the necessary condition for the solution to the S-COPCP, i.e., (V^*, D^*) should satisfy the following equation:

$$0 = \tilde{n}^T Q \tilde{n} + \left(\frac{\partial V^*}{\partial \tilde{n}}\right)^T \mathbf{F} + \left(\frac{\partial V^*}{\partial \tilde{n}}\right)^T \mathbf{S} \bar{v} + \underline{v}^T R \ln(\mathbf{1}_{\alpha_u} - \tanh^2(D^*)) \quad (21)$$

where $\mathbf{1}_{\alpha_u} \in \mathbb{R}^{\alpha_u}$ is a column vector with each element equal to 1.

■

The proof of Lemma 3.1 is presented in Appendix B. Note that (21) is the HJB equation for the S-COPCP of the multi-region MFD system. To find the optimal feedback control policy \tilde{u}^* that minimizes (15), it is necessary to solve the HJB equation (21) for the value function V^* and unconstrained control D^* , and then substitute them into (20). However, the HJB equation (21) is extremely difficult to solve due to its strong nonlinearity. In the subsequent sections, a data-driven online algorithm will be presented to find an approximate solution to (21) without requiring the system dynamics.

MinTTS COPCP (T-COPCP) of the Multi-region MFD System

Another commonly adopted perimeter control objective is to minimize the total time spent (TTS) during the simulation period:

$$\min_u \bar{J}(n_0) = \int_0^{t_f} \left(\sum_{i=1}^L n_i(t) + \bar{\lambda} \|u(t)\| \right) dt \quad (22)$$

subject to (12)

where n and u are constrained by (11a)-(11b). The last term of the value function (22) is to damp oscillation of the control input, where $\bar{\lambda}$ is a positive constant to adjust the weight of the norm. Different from S-COPCP, the formulation of T-COPCP does not require coordinate transformation.

The Hamiltonian function can be formulated as:

$$\bar{H}\left(n, u, \frac{\partial \bar{V}}{\partial n}\right) = \sum_{i=1}^L n_i(t) + \bar{\lambda} \|u(t)\| + \left(\frac{\partial \bar{V}}{\partial n}\right)^T \cdot (F(n) + S(n)u) \quad (23)$$

where $\bar{V}(n(t)) = \int_0^{t_f} \left(\sum_{i=1}^L n_i(\tau) + \bar{\lambda} \|u(\tau)\| \right) d\tau$.

Similar to the deduction of Lemma 3.1, the corresponding constrained optimal control law is

$$u^* = -\underline{v}' \odot \tanh(\bar{D}^*) + \bar{v}', \text{ with } \bar{D}^* = \frac{1}{\underline{v}'} \odot \left(\frac{1}{2\bar{\lambda}} S^T \frac{\partial \bar{V}^*}{\partial n} \right) \quad (24)$$

where $\bar{v}' \triangleq [\bar{v}'_1, \dots, \bar{v}'_{\alpha_u}]^T \in \mathbb{R}^{\alpha_u}$, $\underline{v}' \triangleq [\underline{v}'_1, \dots, \underline{v}'_{\alpha_u}]^T \in \mathbb{R}^{\alpha_u}$ with $\bar{v}'_{k_u} = \frac{u_{k_u}^{\max} + u_{k_u}^{\min}}{2}$, $\underline{v}'_{k_u} = \frac{u_{k_u}^{\max} - u_{k_u}^{\min}}{2}$.

Note that (12) and (14) are in the same affine form. The theoretical results developed for system (14) (regarding S-COPCP) can be applied to system (12) (regarding T-COPCP).

4. Data-driven IRL based adaptive optimal perimeter control

Parallel to the development in Section 2, to relax the requirement of system knowledge and consider sensor data measurements, we will establish an equivalent formulation of the HJB equation (21) that does not involve the system dynamics. Towards this, in this section a recapitulation of the policy iteration method for solving (21) will be presented. Based on the policy iteration method, a data-driven model-free adaptive optimal perimeter controller, which considers the heterogeneous discrete-time sensor data, is developed through the lens of the integral reinforcement learning (IRL).

Note that it is difficult to give an analytical solution to (21) due to the strong nonlinearity. Policy iteration is one of the most common methods to resolve this difficulty. The policy iteration method considering heterogeneous cross-boundary capacities is as follows:

1. (Policy evaluation) Given an initial admissible control policy $\tilde{u}^0(\tilde{n})$, find $V^k(\tilde{n})$ successively approximated by solving the following equation with $V^k(0) = 0$

$$\mathcal{L}(\tilde{n}, \tilde{u}^k) + \left(\frac{\partial V^{k+1}}{\partial \tilde{n}} \right)^T (\mathbf{F} + \mathbf{S}\tilde{u}^k) = 0, k = 0, 1, \dots \quad (25)$$

2. (Policy improvement) Update the control policy simultaneously by

$$\tilde{u}^{k+1}(\tilde{n}) = -\underline{v} \odot \tanh(D^{k+1}) + \bar{v}, D^{k+1} = \frac{1}{2\underline{v}} \odot \left(R^{-1} \mathbf{S}^T \frac{\partial V^{k+1}}{\partial \tilde{n}} \right) \quad (26)$$

where k is the iterative index. The policy evaluation is implemented to update the iterative value function that satisfies the Bellman equation (19). Then based on value iteration, the policy improvement is implemented to obtain the iterative control law sequence that minimizes the total cost in each period. From the policy improvement, we can always find another control law sequence that is better, or at least no worse. The following lemma demonstrates the convergence of V^k and \tilde{u}^k (i.e., D^k) by iterating (25)-(26) to the optimal value function V^* and optimal perimeter control \tilde{u}^* (i.e., D^*).

Lemma 4.1. Let $V^k(\tilde{n}) \in C^1(\Omega)$ on Ω where $V^k(\tilde{n}) \geq 0$, $V^k(0) = 0$ and $\tilde{u}^k(\tilde{n})$ is admissible to (14), $k = 0, 1, \dots$. If $(V^{k+1}(\tilde{n}), \tilde{u}^k(\tilde{n}))$ and $(V^{k+2}(\tilde{n}), \tilde{u}^{k+1}(\tilde{n}))$ both satisfy (19) with the boundary condition $V^{k+1}(0) = 0$, $V^{k+2}(0) = 0$, then

- 1) the obtained control policies $\tilde{u}^{k+1}(\tilde{n})$ in (26) are admissible for (14) on Ω ;
- 2) $V^*(\tilde{n}) \leq V^{k+2}(\tilde{n}) \leq V^{k+1}(\tilde{n})$, $\forall \tilde{n} \in \Omega$;
- 3) $\lim_{k \rightarrow \infty} V^k(\tilde{n}) = V^*(\tilde{n})$;
- 4) $\lim_{k \rightarrow \infty} \tilde{u}^k(\tilde{n}) = \tilde{u}^*(\tilde{n})$.

■

We present the proof of Lemma 4.1 in Appendix C.

Lemma 4.1 indicates that using the policy iteration method, (V^k, \tilde{u}^k) (i.e., (V^k, D^k)) can approximate the optimal solution (V^*, \tilde{u}^*) (i.e., (V^*, D^*)) to the HJB equation (21). However, (25)-(26) requires identification of the MFD dynamics \mathbf{F} and \mathbf{S} . To enable a data-driven method without requiring calibration of the MFD dynamics (14), the main idea is to get rid of the system dynamics in the HJB equation (21). We can adopt an off-policy IRL algorithm that the control implemented can be different from the optimal control (26). Towards this, we rewrite the traffic dynamics (14) as

$$\dot{\tilde{n}} = \mathbf{F}(\tilde{n}) + \mathbf{S}(\tilde{n})\tilde{u}^k + \mathbf{S}(\tilde{n})(\tilde{u} - \tilde{u}^k) \quad (27)$$

where \tilde{u}^k is the policy to be updated and \tilde{u} is the behavior policy that is actually implemented to the system dynamics to generate the data for learning.

Remark 4.1. On-policy and off-policy are two important RL methods. The policy iteration (25)-(26) can be regarded as a class of on-policy methods. When using the on-policy methods, the learned control policy should be applied to generate data simultaneously even before it converges. Although the on-policy methods can provide nearly unbiased estimates of the policy gradient, they (e.g., Sarsa) are usually data-intensive and their learning process is time-consuming. Furthermore, the data usage of on-policy learning methods is low because the samples generated previously would be discarded along with each policy changes. Thus, the implementation of on-policy learning method is generally difficult. Unlike the on-policy learning, the off-policy learning evaluates the target policy when executing other behavior policies.

There are several practical reasons that the implemented control can differ from the optimal control to be learned. As discussed in Zhong et al. (2018b), the traffic managers may have difficulties in calibrating a detailed functional form and its steady state for the time-varying travel demand and the MFD dynamics. Thus, they may not be able to implement the model-based optimal control (that is a ‘miracle’ to the manager) in the learning process. On the other hand, the traffic managers definitely have a preferable network condition (or state) for management purposes. The implemented control \tilde{u} can be arbitrary enables the traffic managers to enforce their preference as a ‘priori’ for traffic management purposes. This can be regarded as a superiority of the proposed off-policy IRL-based learning algorithms. This implemented control can stimulate the network dynamics so that the learning algorithms can observe the evolution of traffic states and the network performance to adjust the adaptive optimal control iteratively. ■

Now we derive the IRL Bellman equation that does not involve the system dynamics \mathbf{F} and \mathbf{S} , i.e., “model-free”.

The time derivative of $V^{k+1}(\tilde{n}(t))$ for the $\{k+1\}$ -th iteration equals

$$\frac{dV^{k+1}}{dt} = \left(\frac{\partial V^{k+1}}{\partial \tilde{n}} \right)^T (\mathbf{F} + \mathbf{S}\tilde{u}) \quad (28)$$

Subtracting (25) from (28), we have

$$\frac{dV^{k+1}}{dt} = \left(\frac{\partial V^{k+1}}{\partial \tilde{n}} \right)^T (\mathbf{F} + \mathbf{S}\tilde{u}) - \left(\frac{\partial V^{k+1}}{\partial \tilde{n}} \right)^T (\mathbf{F} + \mathbf{S}\tilde{u}^k) - \mathcal{L}(\tilde{n}, \tilde{u}^k) = \left(\frac{\partial V^{k+1}}{\partial \tilde{n}} \right)^T \mathbf{S}(\tilde{u} - \tilde{u}^k) - \mathcal{L}(\tilde{n}, \tilde{u}^k) \quad (29)$$

From the second equation of (26), we have

$$\begin{aligned} 2\underline{v} \odot D^{k+1} &= R^{-1} \mathbf{S}^T \frac{\partial V^{k+1}}{\partial \tilde{n}} \\ \Rightarrow \left(\frac{\partial V^{k+1}}{\partial \tilde{n}} \right)^T \mathbf{S} R^{-1} &= (2\underline{v} \odot D^{k+1})^T \\ \Rightarrow \left(\frac{\partial V^{k+1}}{\partial \tilde{n}} \right)^T \mathbf{S} &= 2(\underline{v} \odot D^{k+1})^T R \end{aligned} \quad (30)$$

Substituting (30) into (29) yields

$$\frac{dV^{k+1}}{dt} = 2(\underline{v} \odot D^{k+1})^T R(\tilde{u} - \tilde{u}^k) - \mathcal{L}(\tilde{n}, \tilde{u}^k) \quad (31)$$

Integrating both sides of (31) on the interval $[t, t + \Delta t]$, we obtain

$$\begin{aligned} V^{k+1}(\tilde{n}(t + \Delta t)) - V^{k+1}(\tilde{n}(t)) &= \int_t^{t+\Delta t} 2(\underline{v} \odot D^{k+1})^T R(\tilde{u} - \tilde{u}^k) d\tau - \int_t^{t+\Delta t} \mathcal{L}(\tilde{n}, \tilde{u}^k) d\tau \\ \Rightarrow V^{k+1}(\tilde{n}(t)) &= \int_t^{t+\Delta t} \mathcal{L}(\tilde{n}, \tilde{u}^k) d\tau - \int_t^{t+\Delta t} 2(\underline{v} \odot D^{k+1})^T R(\tilde{u} - \tilde{u}^k) d\tau + V^{k+1}(\tilde{n}(t + \Delta t)) \end{aligned} \quad (32)$$

for any time $t \geq 0$ and time interval $\Delta t > 0$. As introduced in Section 2, Δt is termed as the reinforcement interval. There is a trade-off between the learning rate and the reinforcement interval. It is found by Modares et al. (2014) that the larger the reinforcement interval Δt is, the smaller the learning rate should be chosen.

(32) is called IRL Bellman equation, which no longer involves the model information of the traffic dynamics. Thus, solving (32) instead of the HJB equation (21), we can obtain a data-driven IRL based adaptive optimal perimeter controller, which is “model-free”.

Note that the convergence of the iteration sequence $\{(V^{k+1}, D^{k+1})\}$ by using (25)-(26) to the optimality has been checked by Lemma 4.1. Hence, we only need to justify the equivalence between the policy iterative equations (25)-(26) and the IRL Bellman equation (32), whereby the convergence and optimality of the IRL approach can also be derived.

Theorem 4.1. The IRL Bellman equation (32) gives the same solution to the value function as the Bellman equation (25) and the same updated control policy as (26). ■

Proof. The proof of Theorem 4.1 is divided into two fold.

1) First, we prove that (25)-(26) \Rightarrow (32). Provided that (V^{k+1}, D^{k+1}) is the solution of the policy iterative equations (25)-(26), from the derivation of (32), one can easily deduce that (V^{k+1}, D^{k+1}) is the solution of (32).

2) Next, we prove that (32) \Rightarrow (25)-(26). Provided that (V^{k+1}, D^{k+1}) is the solution of the IRL Bellman equation (32) and that $D^{k+1} = \frac{1}{2\underline{v}} \odot \left(R^{-1} \mathbf{S}^T \frac{\partial V^{k+1}}{\partial \tilde{n}} \right)$.

Dividing both sides of (32) by Δt and taking limit results in

$$\begin{aligned} \lim_{\Delta t \rightarrow 0} \frac{V^{k+1}(\tilde{n}(t + \Delta t)) - V^{k+1}(\tilde{n}(t))}{\Delta t} &= \lim_{\Delta t \rightarrow 0} \frac{\int_t^{t+\Delta t} 2(\underline{v} \odot D^{k+1})^T R(\tilde{u} - \tilde{u}^k) d\tau - \int_t^{t+\Delta t} \mathcal{L}(\tilde{n}, \tilde{u}^k) d\tau}{\Delta t} \\ \Rightarrow \frac{dV^{k+1}}{dt} &= 2(\underline{v} \odot D^{k+1})^T R(\tilde{u} - \tilde{u}^k) - \mathcal{L}(\tilde{n}, \tilde{u}^k) \end{aligned} \quad (33)$$

Substituting $D^{k+1} = \frac{1}{2\underline{v}} \odot (R^{-1} \mathbf{S}^T \frac{\partial V^{k+1}}{\partial \tilde{n}})$ into (33), we have

$$\frac{dV^{k+1}}{dt} = \left(\frac{\partial V^{k+1}}{\partial \tilde{n}} \right)^T \mathbf{S}(\tilde{u} - \tilde{u}^k) - \mathcal{L}(\tilde{n}, \tilde{u}^k) \quad (34)$$

Combining (27) and (34), it follows that

$$\begin{aligned} \frac{dV^{k+1}}{dt} &= \left(\frac{\partial V^{k+1}}{\partial \tilde{n}} \right)^T \mathbf{S}(\tilde{u} - \tilde{u}^k) - \mathcal{L}(\tilde{n}, \tilde{u}^k) + \left(\frac{\partial V^{k+1}}{\partial \tilde{n}} \right)^T \mathbf{F} - \left(\frac{\partial V^{k+1}}{\partial \tilde{n}} \right)^T \mathbf{F} \\ &= \left(\frac{\partial V^{k+1}}{\partial \tilde{n}} \right)^T (\mathbf{F} + \mathbf{S}\tilde{u}) - \left(\frac{\partial V^{k+1}}{\partial \tilde{n}} \right)^T (\mathbf{F} + \mathbf{S}\tilde{u}^k) - \mathcal{L}(\tilde{n}, \tilde{u}^k) \\ &\Rightarrow \mathcal{L}(\tilde{n}, \tilde{u}^k) + \left(\frac{\partial V^{k+1}}{\partial \tilde{n}} \right)^T (\mathbf{F} + \mathbf{S}\tilde{u}^k) = \left(\frac{\partial V^{k+1}}{\partial \tilde{n}} \right)^T (\mathbf{F} + \mathbf{S}\tilde{u}) - \frac{dV^{k+1}}{dt} \end{aligned} \quad (35)$$

From (28) we have the right side of (35) equals to 0. Hence,

$$\mathcal{L}(\tilde{n}, \tilde{u}^k) + \left(\frac{\partial V^{k+1}}{\partial \tilde{n}} \right)^T (\mathbf{F} + \mathbf{S}\tilde{u}^k) = 0 \quad (36)$$

(36) is the same as (25). This completes the proof. \blacksquare

□

Note that we have proven the equivalence between the Bellman equation and the IRL Bellman equation, which does not involve the traffic dynamics (model-free). By iterating V^k on the IRL Bellman equation and updating the control policy D^k (i.e., \tilde{u}^k), we can approach both the optimal value function V^* and the optimal perimeter control \tilde{u}^* . In the subsequent section, we will develop an online learning approach via the IRL Bellman equation (32) to approximate the optimal value function and perimeter controller.

5. Online learning by integrating experience replay

For the implementation of the conventional off-line learning based RL approach, sufficient historical data must be collected beforehand and the collected data set would be used repeatedly during the learning process. This implies that only recurrent traffic conditions can be well handled by the conventional off-line learning based RL approach. To adapt to new or unseen data samples and possible changes of traffic conditions, an online iterative learning approach based on the IRL is proposed in this section. Employing off-policy methods, the proposed online learning approach can be integrated with the ER technique to reduce the requirement on real-time data samples and simultaneously reduce the computational burden.

The online (incorporated with ER) learning method is constructed via the actor-critic (AC) neural network (NN) framework. The neural networks can learn the unknown macroscopic traffic dynamics and achieve the adaptive optimal perimeter control with the IRL. The critic (i.e., policy evaluation) NN and the actor (i.e., policy improvement) NN are tuned sequentially. The flow chart of the proposed IRL algorithm is shown in Figure 3. The algorithm starts by evaluating the cost of a given initial admissible control policy and then uses this information to obtain a new and improved control policy that generates a lower associated cost than the previous one does. These two steps of policy evaluation and policy improvement are repeated until the actual policy remains unchanged after the policy improvement step, whereby the convergence to the optimal controller is achieved. The convergence and stability analysis are evidenced via the Lyapunov theory.

Accordingly, at any time $t > \Delta t$ with reinforcement interval $\Delta t > 0$, given that \tilde{u}' is an admissible control, the IRL Bellman equation (32) can thus be rewritten as follows

$$V(\tilde{n}(t - \Delta t)) = \int_{t-\Delta t}^t \mathcal{L}(\tilde{n}(\tau), \tilde{u}'(\tau)) d\tau - \int_{t-\Delta t}^t 2(\underline{v} \odot D(\tau))^T R(\tilde{u} - \tilde{u}'(\tau)) d\tau + V(\tilde{n}(t)) \quad (37)$$

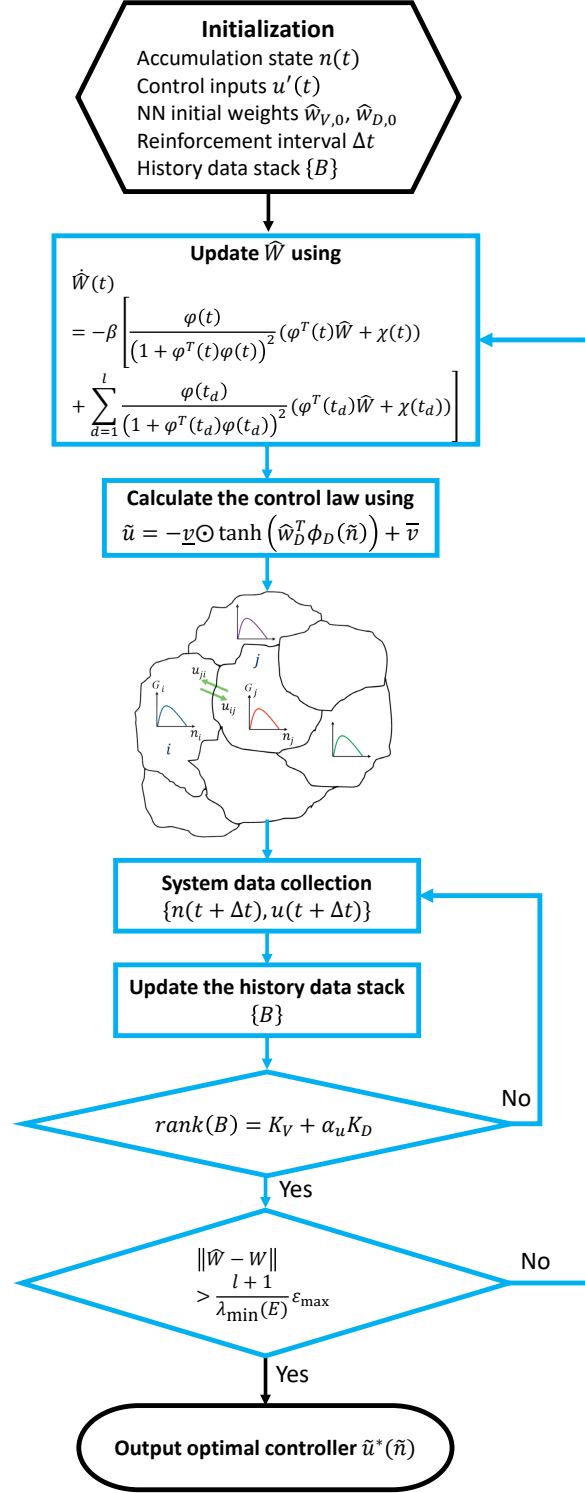


Figure 3: The online iterative learning algorithm

We utilize an AC-NN framework to approximate the value function and the control policy (i.e., the solution of (37)) simultaneously:

$$V(\tilde{n}) = w_V^T \phi_V(\tilde{n}) + \varepsilon_V(\tilde{n}), \quad D(\tilde{n}) = w_D^T \phi_D(\tilde{n}) + \varepsilon_D(\tilde{n}) \quad (38)$$

where $\phi_V : \mathbb{R}^{\alpha_n} \rightarrow \mathbb{R}^{K_V}$, $\phi_D : \mathbb{R}^{\alpha_n} \rightarrow \mathbb{R}^{K_D}$ are vectors of linearly independent activation functions, $w_V^T \in \mathbb{R}^{K_V}$, $w_D^T \in \mathbb{R}^{K_D \times \alpha_u}$ are the NN weights of appropriate dimensions, $\varepsilon_V(\tilde{n})$ and $\varepsilon_D(\tilde{n})$ are the approximation errors of the critic NN and the actor NN, respectively.

Using the approximations (38) in (37) and considering $\varepsilon_V = 0$, $\varepsilon_D = 0$ for the ideal weights w_V and w_D , one has

$$\varepsilon_B(t) \triangleq \int_{t-\Delta t}^t \mathcal{L}(\tilde{n}(\tau), \tilde{u}'(\tau)) d\tau - \int_{t-\Delta t}^t 2(\underline{v} \odot w_D^T \phi_D(\tilde{n}(\tau)))^T R(\tilde{u} - \tilde{u}'(\tau)) d\tau + w_V^T (\phi_V(\tilde{n}(t)) - \phi_V(\tilde{n}(t - \Delta t))) \quad (39)$$

where $\varepsilon_B(t)$ is the Bellman equation error at time t . ε_B is assumed to be bounded on the compact set Ω given the ideal weights w_V and w_D (Modares et al., 2014). That is, there exists a bound ε_{\max} such that $\|\varepsilon_B\| \leq \varepsilon_{\max}$.

Note that the ideal weights w_V and w_D that provide the best approximate solution for (39) are unknown. Hence, the estimations of value function and control policy are given by

$$\hat{V}(\tilde{n}) = \hat{w}_V^T \phi_V(\tilde{n}), \quad \hat{D}(\tilde{n}) = \hat{w}_D^T \phi_D(\tilde{n}) \quad (40)$$

where $\hat{w}_V \in \mathbb{R}^{K_V}$, $\hat{w}_D \in \mathbb{R}^{K_D \times \alpha_u}$ are estimations of w_V and w_D , respectively. These estimations are usually learned from training data.

Using (40) in (37), the approximation error of the IRL Bellman equation, i.e., the TD error, at time t is given by

$$\begin{aligned} e(t) &= \hat{V}(\tilde{n}(t)) - \hat{V}(\tilde{n}(t - \Delta t)) - \int_{t-\Delta t}^t 2(\underline{v} \odot \hat{D}(\tau))^T R(\tilde{u} - \tilde{u}'(\tau)) d\tau + \int_{t-\Delta t}^t \mathcal{L}(\tilde{n}(\tau), \tilde{u}'(\tau)) d\tau \\ &= \phi_V^T(\tilde{n}(t)) \hat{w}_V - \phi_V^T(\tilde{n}(t - \Delta t)) \hat{w}_V - \int_{t-\Delta t}^t 2(\underline{v} \odot (\hat{w}_D^T \phi_D(\tilde{n}(\tau))))^T R(\tilde{u} + \underline{v} \odot \tanh(\hat{w}_D^T \phi_D(\tilde{n}(\tau))) - \bar{v}) d\tau \\ &\quad + \int_{t-\Delta t}^t \left(\tilde{n}^T(\tau) Q \tilde{n}(\tau) + 2\underline{v}^T R \int_{\bar{v}}^{-\underline{v} \odot \tanh(\hat{w}_D^T \phi_D(\tilde{n}(\tau))) + \bar{v}} \tanh^{-1} \left(\frac{1}{\underline{v}} \odot (v - \bar{v}) \right) dv \right) d\tau \end{aligned} \quad (41)$$

Let $\hat{W} = [\hat{w}_V^T, \text{vec}^T(\hat{w}_D)]^T \in \mathbb{R}^{K_V + \alpha_u K_D}$ be the estimated weight of the AC-NNs, where $\text{vec}(\hat{w}_D) \in \mathbb{R}^{\alpha_u K_D}$ is the vectorization of matrix $\hat{w}_D \in \mathbb{R}^{K_D \times \alpha_u}$. Thus, (41) can be rewritten as

$$e(t) = \varphi^T(\tilde{n}(t), \tilde{u}(t)) \hat{W} + \chi(\tilde{n}(t)) \quad (42)$$

where

$$\begin{aligned} \varphi(\tilde{n}(t), \tilde{u}(t)) &= \left[\int_{t-\Delta t}^t (2\underline{v} \odot R(\tilde{u} + \underline{v} \odot \tanh(\hat{w}_D^T \phi_D(\tilde{n}(\tau))) - \bar{v})) \otimes \phi_D(\tilde{n}(\tau)) d\tau \right] \\ \chi(\tilde{n}(t)) &= \int_{t-\Delta t}^t \mathcal{L}(\tilde{n}(\tau), \tilde{u}'(\tau)) d\tau = \int_{t-\Delta t}^t \left(\tilde{n}^T(\tau) Q \tilde{n}(\tau) + 2\underline{v}^T R \int_{\bar{v}}^{-\underline{v} \odot \tanh(\hat{w}_D^T \phi_D(\tilde{n}(\tau))) + \bar{v}} \tanh^{-1} \left(\frac{1}{\underline{v}} \odot (v - \bar{v}) \right) dv \right) d\tau \end{aligned}$$

To enable online learning, we use the gradient-descent method to update the estimated AC-NN weights. Both real-time data and historical data are used to estimate the weights of the NNs to guarantee the data richness and efficiency.

As discussed in Section 2, the ER technique can be integrated with the IRL algorithm to speed up the computation. Based on the generalized least-squares (GLS) principle, we aim to update the estimated weight vector \hat{W} to minimize $\|e(t)\| + \sum_{d=1}^l \|e(t_d)\|$, where the first part denotes the instantaneous TD error and the second part denotes the TD errors for the stored transition samples. In order to ensure the existence of the solution, we need the following assumption.

Assumption 5.1. Define $B = [\varphi(t_1), \dots, \varphi(t_l)]$ as a matrix of the stored data, where l is the number of samples stored in the history stack. There are as many linearly independent elements as the number of corresponding NN's hidden neurons for the stored data matrix B such that $\text{rank}(B) = K_V + \alpha_u K_D$.

This rank condition is to verify the richness of the stored data, i.e., whether it is sufficient to solve the GLS problem and to guarantee the convergence to a near-optimal control (Modares et al., 2014). Based on (42), for the online iterative learning, the gradient-based adaptation law with ER is given by

$$\begin{aligned}\dot{\hat{W}}(t) &= -\beta \left(\frac{\varphi(t)}{(1 + \varphi^T(t)\varphi(t))^2} e(t) + \sum_{d=1}^l \frac{\varphi(t_d)}{(1 + \varphi^T(t_d)\varphi(t_d))^2} e(t_d) \right) \\ &= -\beta \left(\frac{\varphi(t)}{(1 + \varphi^T(t)\varphi(t))^2} (\varphi^T(t)\hat{W} + \chi(t)) + \sum_{d=1}^l \frac{\varphi(t_d)}{(1 + \varphi^T(t_d)\varphi(t_d))^2} (\varphi^T(t_d)\hat{W} + \chi(t_d)) \right)\end{aligned}\quad (43)$$

where $\beta > 0$ is the learning rate, t is the current time and the index d refers to the d -th sample data ($d = 1, \dots, l$) stored in the history stack B . In (43), the first term is a gradient-descent update law for minimizing $\|e(t)\|$, while the second term attempts to minimize $\sum_{d=1}^l \|e(t_d)\|$.

Denote the optimal value of weight by $W = [w_V^T, \text{vec}^T(w_D)]^T$ and recall that the estimated weight is defined by $\hat{W} = [\hat{w}_V^T, \text{vec}^T(\hat{w}_D)]^T$. The following theorem demonstrates the convergence of the weight estimation error of AC-NNs, $\tilde{W}(t) = W - \hat{W}(t)$, using Lyapunov method.

Theorem 5.1. If the stored data B for AC-NNs (40) with the ER adaptation law (43) satisfy Assumption 5.1,

- 1) for bounded ε_B , the weight estimation error $\tilde{W}(t) = W - \hat{W}(t)$ converges exponentially to the residual set $R_s = \{\tilde{W} \mid \|\tilde{W}(t)\| \leq c \cdot \varepsilon_{\max}\}$, where $c > 0$ is a constant;
- 2) the system state \tilde{n} is asymptotically stable.

■

Proof. 1) Based on (39), (41), (42) and $\tilde{W}(t) = W - \hat{W}(t)$, the TD errors for the current time t and the recorded time t_d can be rewritten respectively as

$$e(t) = \varphi^T(t)\hat{W} + \chi(t) = \varphi^T(t)W - \varphi^T(t)\tilde{W} + \chi(t) = -\varphi^T(t)\tilde{W} + (\chi(t) + \varphi^T(t)W) = -\varphi^T(t)\tilde{W} + \varepsilon_B(t) \quad (44a)$$

$$e(t_d) = \varphi^T(t_d)\hat{W} + \chi(t_d) = \varphi^T(t_d)W - \varphi^T(t_d)\tilde{W} + \chi(t_d) = -\varphi^T(t_d)\tilde{W} + (\chi(t_d) + \varphi^T(t_d)W) = -\varphi^T(t_d)\tilde{W} + \varepsilon_B(t_d) \quad (44b)$$

From $\tilde{W}(t) = W - \hat{W}(t)$, one has $\dot{\tilde{W}}(t) = -\dot{\hat{W}}(t)$. Substituting (44a)-(44b) into (43) and denoting $\bar{\varphi} = \varphi/(1 + \varphi^T\varphi)$ and $m = 1 + \varphi^T\varphi$, we can obtain

$$\begin{aligned}\dot{\tilde{W}}(t) &= \beta \left(\frac{\varphi(t)}{(1 + \varphi^T(t)\varphi(t))^2} e(t) + \sum_{d=1}^l \frac{\varphi(t_d)}{(1 + \varphi^T(t_d)\varphi(t_d))^2} e(t_d) \right) \\ &= \beta \left(\frac{\bar{\varphi}(t)}{m(t)} (-\varphi^T(t)\tilde{W} + \varepsilon_B(t)) + \sum_{d=1}^l \frac{\bar{\varphi}(t_d)}{m(t_d)} (-\varphi^T(t_d)\tilde{W} + \varepsilon_B(t_d)) \right) \\ &= -\beta \left(\frac{\bar{\varphi}(t)}{m(t)} \varphi^T(t) + \sum_{d=1}^l \frac{\bar{\varphi}(t_d)}{m(t_d)} \varphi^T(t_d) \right) \tilde{W} + \beta \left(\frac{\bar{\varphi}(t)}{m(t)} \varepsilon_B(t) + \sum_{d=1}^l \frac{\bar{\varphi}(t_d)}{m(t_d)} \varepsilon_B(t_d) \right) \\ &= -\beta \left(\bar{\varphi}(t)\bar{\varphi}^T(t) + \sum_{d=1}^l \bar{\varphi}(t_d)\bar{\varphi}^T(t_d) \right) \tilde{W} + \beta \bar{\varepsilon}_B\end{aligned}\quad (45)$$

where $\bar{\varepsilon}_B = \frac{\bar{\varphi}(t)}{m(t)} \varepsilon_B(t) + \sum_{d=1}^l \frac{\bar{\varphi}(t_d)}{m(t_d)} \varepsilon_B(t_d)$.

Now we choose the Lyapunov function as

$$L = \frac{1}{2\beta} \tilde{W}^T(t)\tilde{W}(t) \quad (46)$$

Differentiating (46) along the trajectories of (45), one has

$$\begin{aligned}
\dot{L} &= \frac{1}{\beta} \tilde{W}^T \dot{\tilde{W}} \\
&= \frac{1}{\beta} \tilde{W}^T \cdot \left(-\beta \left(\bar{\varphi}(t) \bar{\varphi}^T(t) + \sum_{d=1}^l \bar{\varphi}(t_d) \bar{\varphi}^T(t_d) \right) \tilde{W} + \beta \bar{\varepsilon}_B \right) \\
&= -\tilde{W}^T \left(\bar{\varphi}(t) \bar{\varphi}^T(t) + \sum_{d=1}^l \bar{\varphi}(t_d) \bar{\varphi}^T(t_d) \right) \tilde{W} + \tilde{W}^T \bar{\varepsilon}_B
\end{aligned} \tag{47}$$

If [Assumption 5.1](#) is satisfied, then $\bar{\varphi}(t) \bar{\varphi}^T(t) + \sum_{d=1}^l \bar{\varphi}(t_d) \bar{\varphi}^T(t_d) > 0$. Suppose that ε_B is bounded by ε_{\max} , i.e., $\|\varepsilon_B\| \leq \varepsilon_{\max}$, \dot{L} is negative definite provided that

$$\|\tilde{W}(t)\| > \frac{l+1}{\lambda_{\min}(E)} \varepsilon_{\max} = c \cdot \varepsilon_{\max} \tag{48}$$

where $c = \frac{l+1}{\lambda_{\min}(E)} > 0$ and $\lambda_{\min}(E)$ is the minimum eigenvalue of E with $E = \bar{\varphi}(t) \bar{\varphi}^T(t) + \sum_{d=1}^l \bar{\varphi}(t_d) \bar{\varphi}^T(t_d)$. Hence, the weight estimation error \tilde{W} converges exponentially to the residual set $R_s = \{\tilde{W} \mid \|\tilde{W}(t)\| \leq c \cdot \varepsilon_{\max}\}$.

2) For system (14), define Lyapunov function candidate as (18). Take the time derivative of V and we can obtain

$$\dot{V} = -\mathcal{L}(\tilde{n}, \tilde{u}) = -N(\tilde{n}) - U(\tilde{u})$$

Recall that $N(\tilde{n})$ and $U(\tilde{u})$ are positive definite functions. Then we have $V(\tilde{n}(t)) \geq 0$, $\dot{V} \leq 0$ and $V(\tilde{n}(t)) = 0$ if and only if $\tilde{n} = 0$, i.e., $n = n^*$. That is, $V(\tilde{n})$ is a Lyapunov function. The closed-loop system is thus asymptotically stable. This completes the proof. \blacksquare

[Theorem 5.1](#) indicates that using the gradient-based adaptation law with ER (43), the AC-NN framework (40) can approximate the optimal value function $V^*(\tilde{n})$ and perimeter control policy $\tilde{u}^*(\tilde{n})$. The value function (18) is proven to be a Lyapunov function for the MFD dynamics. Hence, the initial accumulation state n_0 can be asymptotically stabilized by the obtained perimeter controller at the desired steady state n^* .

6. Numerical experiments

6.1. Settings of the test environment

To test the performance of the proposed method, two scenarios with different purposes and settings are simulated (see [Table 2](#)). The network topologies used in these numerical examples are shown in [Figure 4](#). For set-point control objective, the two-region MFD system ([Haddad, 2015](#)) with constant demand pattern is considered in Scenario 1 for demonstration of the convergent speed and computation efficiency of the proposed method. For min TTS control objective, a three-region MFD system as in [Zhong et al. \(2018b\)](#) with time-varying travel demand is considered in Scenario 2. The robustness and adaptiveness of the proposed method are validated by conducting experiments under various demand patterns. The subregion MFD functions of all the examples are assumed to be the same. The true, but unknown MFD functions and the parameters are given in [Table 2](#) to generate the I/O data for learning the traffic dynamics only. Note that they are not involved in the controller design. For the examples in Scenario 1, the cost functions $N(\tilde{n}) = \tilde{n}^T Q \tilde{n}$ and $U(\tilde{u})$ is defined by (17), where $Q = 10^{-2} \cdot \mathcal{I}_{\alpha_n}$, $R = \mathcal{I}_{\alpha_u}$ with \mathcal{I}_x denoting the identity matrix of dimension x . For the experiment in Scenario 2, the objective function is defined by (22), where $\bar{\lambda} = 1$.

The stabilizing control law by [Haddad \(2015\)](#) embedded with a sequence of randomly generated deviations is adopted to initialize the online learning algorithm. The AC-NN framework is employed for approximating the optimal value function and control policy in all examples. Let $\phi_V \in \mathbb{R}^{K_V}$ and $\phi_D \in \mathbb{R}^{K_D}$ denote the activation functions of the online learning approach.

For Scenario 1, inspired by [Abu-Khalaf and Lewis \(2005\)](#), we adopt an AC-NN framework with 84 critic NN hidden neurons and 4 actor NN hidden neurons, i.e., $K_V = 84$ and $K_D = 4$. Suppose $x = [x_1, x_2, x_3, x_4]^T$, the activation function of critic NN is

$$\phi_V^{P_V}(x) = x_1^i x_2^j x_3^m x_4^n \tag{49}$$

Table 2: Scenario description

Network	Demand	Controllers	MFD parameters
1-A	2-region	IRL, N-DP	$G_i(n_i) =$
1-B		IRL (various reinforcement intervals)	$\frac{1.4877 \cdot 10^{-7} n_i^3 - 2.9815 \cdot 10^{-3} n_i^2 + 15.0912 n_i}{3600}$ (veh/s)
1-C		IRL, MPC	
2	3-region	time-varying IRL, MPC	$n_i^{jam} = 10000$ (veh), $n_i^{cr} = 3392$ (veh)

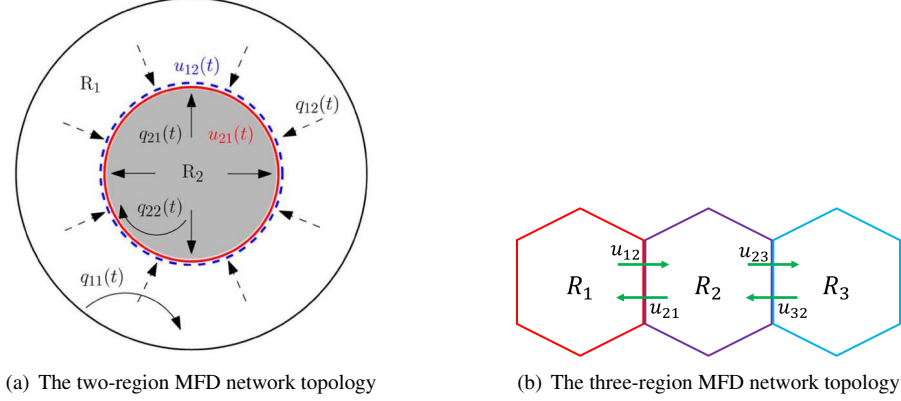


Figure 4: Network topologies

where $i + j + m + n = 6$ and $p_V = 1, \dots, 84$, and the activation function of actor NN is

$$\phi_D^{p_D}(x) = x_{p_D} \quad (50)$$

where $p_D = 1, \dots, 4$.

For Scenario 2, we set $K_V = 210$ and $K_D = 7$. Suppose $x = [x_1, x_2, x_3, x_4, x_5, x_6, x_7]^T$, the activation function of critic NN is

$$\phi_V^{p_V}(x) = x_{k_1}^i x_{k_2}^j x_{k_3}^m x_{k_4}^n \quad (51)$$

where $i + j + m + n = 6$, $p_V = 1, \dots, 210$ and $k_1, k_2, k_3, k_4 \in \{1, \dots, 7\}$, and the activation function of actor NN is

$$\phi_D^{p_D} = x_{p_D} \quad (52)$$

where $p_D = 1, \dots, 7$.

The sample size and replay buffer (history data stack) size for AC-NN updates in all the examples are 250 and 1000, respectively. The computer processor is Intel Core i7-9850 CPU 2.60 GHz, and the simulation platform is MATLAB R2022a.

6.2. Set-point control

In this subsection, we apply the proposed IRL based online iterative learning approach to the two-region network with constant travel demand. A two-region network as shown in Figure 4(a) is considered in this scenario. As explained, the objective of set-point perimeter control is to regulate the network traffic state to the desired stable equilibrium. Comparison in terms of control performance and computational efficiency is made between the proposed IRL approach and other existing controllers, e.g., the state-of-the-art MPC by Geroliminis et al. (2013) and the neurodynamic programming (N-DP) method by Su et al. (2020). Note that MPC is a model-based controller, and that N-DP requires partial information of the MFD system, while the IRL does not rely on any knowledge of the traffic dynamics.

Scenario 1-A: Comparison between the IRL and the N-DP approaches

In Scenario 1-A, we present a comparison between the proposed off-policy learning based IRL approach and the on-policy learning based N-DP approach by Su et al. (2020). In line with Haddad (2015), $\bar{n} = [3000, 3000]^T$ (veh), which is close to the critical accumulation, is chosen as the desired equilibrium. In addition, the demand pattern is set to be constant as $q = [1.6, 1.6, 1.6, 1.6]^T$ (veh/s). Thus, the steady-state accumulation for each direction and the corresponding control inputs as solved from the steady-state equations (13a)–(13c) are $n^* = [1538.9, 1461.1, 1461.1, 1538.9]^T$ (veh) and $u^* = [0.5267, 0.5267]^T$. The initial regional accumulations are set to be $[1800, 3100]^T$ (veh) with OD-specific initial accumulations being $n_{11}(0) = 540$ (veh), $n_{12}(0) = 1260$ (veh), $n_{21} = 2170$ (veh), $n_{22}(0) = 930$ (veh).

Note that N-DP requires input data with high resolution to solve the HJB equation for the optimal controller. For a fair comparison, the first case is that the sample time interval (and thus reinforcement interval) and the control update step are set as 1 second for both methods. To consider more practical situations, in the second case and third case, we set the sample time interval and the control update step to 15 seconds (Haddad, 2015) and 30 seconds, respectively. Sensitivity analysis of the reinforcement interval for the IRL is presented in Scenario 1-B.

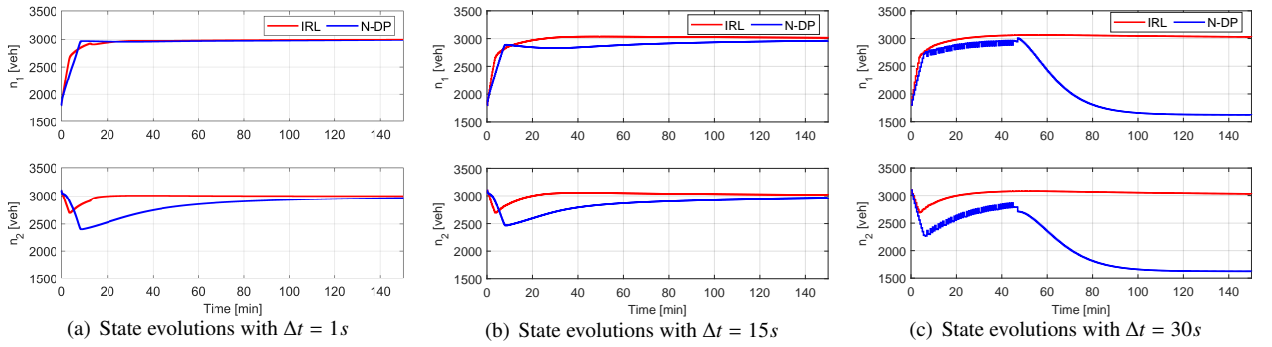


Figure 5: Simulation results of Scenario 1-A

As shown in Figure 5(a), when $\Delta t = 1$, both the IRL and the N-DP can regulate the accumulation states to the desired equilibrium $[3000, 3000]^T$ (veh) in an asymptotic manner. Specifically, the N-DP controller achieves a shorter settling time³ than the IRL approach for accumulation state $n_1(t)$, while the IRL is much better than the N-DP in the settling time for $n_2(t)$. Note that the N-DP control algorithm has been well-trained in an off-line manner before it is applied. However, only by interacting with the environment and learning the macroscopic traffic dynamics online, the proposed IRL approach can achieve settling times of around 20 minutes for both n_1 and n_2 . Besides, $n_2(t)$ has experienced an overshoot to around 2500 (veh) applying the N-DP based controller, while the overshoot induced by the IRL approach is much smaller. Moreover, applying the N-DP, the increase of the reinforcement interval slows down the convergent speed of accumulation states (see Figure 5(b)) or even cannot regulate them to the desired equilibria (see Figure 5(c)). However, the IRL approach can stabilize the accumulations at the desired steady states in all the cases within around 20 minutes. These results indicate that the IRL approach can achieve decent convergence and stability of the accumulation states under different Δt , while the control performance of N-DP deteriorates as Δt increases.

There are also differences in the computational complexity and data usage efficiency. Note that 20000 samples are used for off-line training in each iteration (40 iterations in total) for the N-DP approach, whereas only 250 samples are used in each iteration for the IRL approach. This is the advantage of integrating the ER technique with IRL, i.e., fast convergence of the iterative learning process can be guaranteed. Take the first case as an example, because of the reduction of samples used for each iteration, the total computation time of the IRL approach is less than 8 seconds while that of the N-DP approach is more than 2 minutes. Different from the conventional RL methods (e.g., N-DP) which are usually trained off-line and data intensive, the improvement in data usage efficiency by integrating IRL with ER indicates the real-time applicability of the proposed IRL based perimeter control schemes.

³The settling time is the time required for the dynamics to reach and stay within a small range of certain percentage (usually 5% or 2%) of the desired steady state (see Fig. 3.23 and Chapter 3.4.3 in Franklin et al., 2015). In our case, the settling time is the time required for $\tilde{n}_i(t)$ to reach and stay within 2% of the steady state \bar{n}_i .

Scenario 1-B: Sensitivity analysis of the reinforcement interval

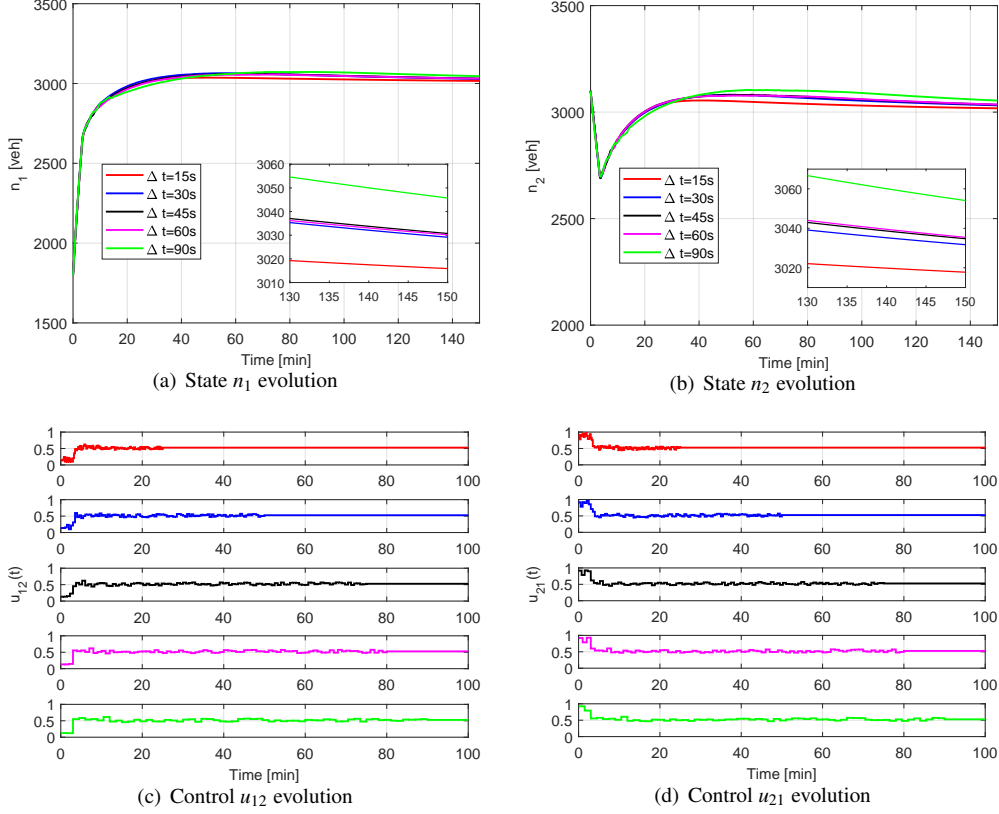


Figure 6: Simulation results of Scenario 1-B with reinforcement intervals equal to control update steps

In Scenario 1-B, sensitivity analysis of the reinforcement interval Δt for the proposed IRL method is performed using the network and settings of Scenario 1-A. We assume that the data resolution of traffic sensors is identical to the reinforcement interval so that one data sample is collected in a reinforcement interval. The larger Δt is, the lower frequency the sensors upload traffic data to the management center. For instance, $\Delta t = 60s$ means the sensors upload data every 1 minute. Note that the larger the reinforcement interval is, the smaller learning rate that could be chosen to achieve the AC-NN weights convergence (Modares et al., 2014). In this example, each learning rate $\beta \in \{0.01, 0.007, 0.005, 0.003, 0.0001, 0.00007\}$ is chosen respectively for each reinforcement interval $\Delta t \in \{15s, 20s, 30s, 45s, 60s, 90s\}$.

Regarding the nature of perimeter control actuation approaches, e.g., traffic signal controls which can be changed only with a new traffic signal cycle, the control update step cannot be smaller than the sample time interval (i.e., the reinforcement interval). Therefore, the sensitivity analysis of reinforcement interval for the IRL algorithm is divided into the following two folds.

The first case is that the control update intervals are equal to the tested reinforcement intervals. Figure 6(a) and Figure 6(b) present the accumulation trajectories $n_1(t)$ and $n_2(t)$ over time under different Δt , respectively, while the control input evolutions are illustrated by Figure 6(c) and Figure 6(d). When $\Delta t = 15s$, the results show that both the initial states and controls converge very fast to the desired equilibrium. As Δt increases, the convergent speed of the perimeter control gain decreases. This slows down the convergent speed of the accumulation states. This is because the algorithm has to wait longer to collect new data to update the weights of the AC-NNs, which also results in less frequent updates of the control inputs. However, Figure 6(a) and Figure 6(b) indicate that the variation of Δt does not significantly influence the convergence of the accumulation states. That is to say, the proposed online learning approach is robust to the variation of real-time data resolution.

Next, we fix the control update steps to 60 seconds while vary the reinforcement intervals in $\Delta t \in \{15s, 20s, 30s, 60s\}$. Figure 7(a)-Figure 7(b) shows that the accumulation states can converge to the desired steady states in around 30 minutes. We can also observe that as Δt increases, both the convergent speeds of the perimeter control gain and the accumulation states decrease. The IRL based perimeter controller with $\Delta t = 15s$ still achieves the shortest settling time. In the early stage of the training and implementation of the IRL controllers, the larger difference between Δt and the control update step, the stronger oscillation of the accumulation state occurs. However, with the control update steps fixed, the variation of Δt still does not significantly affect the convergence of the accumulation states.

These results imply the feasibility of online tuning of the reinforcement interval to adapt to heterogeneous real-time sensor data resolution without affecting the system stability. This is a key advantage of the proposed IRL based online learning algorithm over the traditional RL based methods.

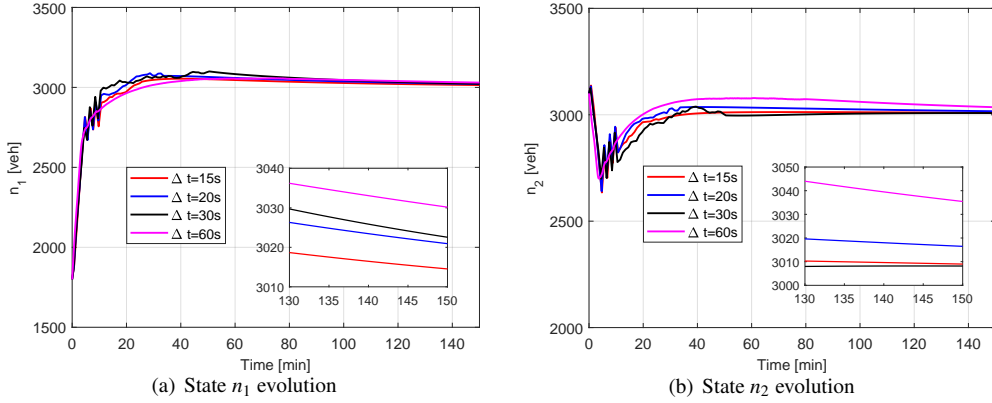


Figure 7: Simulation results of Scenario 1-B with fixed control update steps

Scenario 1-C: Comparison between the IRL and the MPC approaches

Scenario 1-C adopts the same settings as Scenario 1-A except the initial condition, the set-point value and the reinforcement interval. Unlike Scenario 1-A corresponding to a mild traffic condition where all regions are regulated in an uncongested regime (i.e., below the critical accumulation), the initial accumulation state values are set to far exceed the critical accumulations, i.e., $[4300, 3700]^T$ (veh) with $n_{11}(0) = 430$ (veh), $n_{12}(0) = 3870$ (veh), $n_{21} = 370$ (veh), $n_{22}(0) = 3330$ (veh). Besides, in Scenario 1-C, both regions are regulated around set points in the congested regimes, e.g., $\bar{n} = [4000, 4000]^T$ (veh). Performance comparison is conducted between the IRL and the state-of-the-art MPC method, where for both the controllers the sample time interval and the control update step are set as 60 seconds. For the MPC controller, the prediction horizon is set to be 30 (i.e., 30 minutes simulation time).

Figure 8 shows that both the IRL and the MPC controllers can stabilize the accumulation states at the desired equilibrium. Regulated by the IRL controller, both n_1 and n_2 converge very fast to the steady states, while regulated by the MPC controller, one can observe small overshoots of the accumulation states. The settling time and the average CPU time per control update step⁴ of different control schemes are reported in Table 3. Despite no model knowledge available, the IRL approach can achieve a 20-minute settling time, which indicates that the IRL can have a decent control performance in a congested traffic situation. The CPU times per control update step of both methods are extremely small, which are far less than the 60-second control update step. These results imply the real-time applicability of the proposed model-free IRL approach.

6.3. TTS minimization

In this subsection, the objective function is related to minimizing the total time spent (TTS) for the urban network subject to uncertainties in travel demands. We apply the proposed IRL based perimeter controller to the three-region

⁴The CPU time is defined as the average computation time per control update step. They were measured by the tic and toc functions of MATLAB R2022a. We present the average value of 10 tests for each controller.

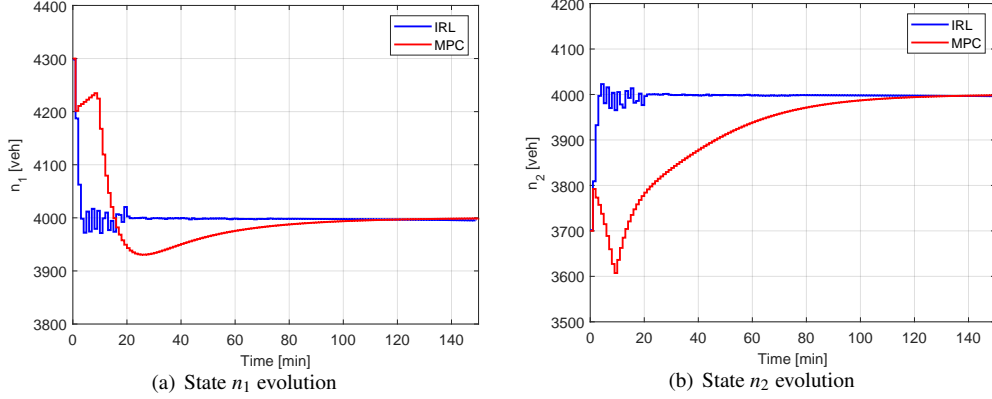


Figure 8: Simulation results of Scenario 1-C

Table 3: Summary of settling time and computation time for Scenario 1-C

	State	IRL	MPC
Settling time (min)	n_1	≈ 22	≈ 29
	n_2	≈ 21	≈ 53
CPU time per step (sec)	–	6.57×10^{-6}	1.79×10^{-2}

network shown by Figure 4(b) with a time-varying demand pattern. The perimeter controller is subject to heterogeneous cross-boundary capacities, i.e.,

$$0.1 \leq u_{12} \leq 0.7, \quad 0.3 \leq u_{21} \leq 1, \quad 0.4 \leq u_{23} \leq 1, \quad 0.2 \leq u_{32} \leq 0.9$$

Scenario 2: Three-region MFD system with uncertain time-varying travel demand

In this scenario, a time-varying demand pattern is used to mimic a scenario of peak-hour traffic with congestion onset, stationary congestion and congestion dissolving processes. Comparisons between the IRL approach and MPC are made under three different travel demand patterns, i.e., 1) the nominal deterministic travel demand pattern (Figure 9(a)), 2) the nominal demand pattern subject to external disturbances (Figure 9(b)), and 3) the travel demand pattern subject to an abrupt change during the stationary congestion period (Figure 9(c)). The initial accumulation state is set as $n(0) = [5400, 5500, 2000]^T$ (veh). Namely, n_1 and n_2 are initiated in a very congested state while n_3 in an uncongested initial state. For both the IRL and the MPC, the control update interval is set as 60 seconds.

The results are given in Figure 9, where the evolution of regional accumulations (Figure 9(d), Figure 9(e) and Figure 9(f) for the nominal, noisy and abrupt-change demand cases, respectively) are shown alongside graphs of control input evolutions (Figure 9(g), Figure 9(h) and Figure 9(i)) and TTS evolutions (Figure 9(j), Figure 9(k) and Figure 9(l)), for the IRL and the MPC schemes. The achieved TTS and the average CPU time per control update step of different control schemes are summarized in Table 4.

Figure 9(d), Figure 9(e) and Figure 9(f) illustrate that in all the demand cases, Region 1 and 2 are congested at the beginning while Region 3 is uncongested, and all the regional accumulation states experience increase during the early stage due to the increase in inflow demands. It is noteworthy that the congestion in Region 3 regulated by the IRL starts to dissipate after 20 minutes, while the accumulation state of Region 3 regulated by MPC continues being increasingly congested. As observed from Figure 9(j), Figure 9(k) and Figure 9(l), the IRL is superior to the MPC in minimizing TTS for the whole network. Based on Table 4, in the abrupt-change demand case, the IRL achieves a 12% decrease in TTS over MPC, while the same performance metrics are 11% and 10% respectively for the nominal and noisy demand cases. These results demonstrate that the proposed IRL based control strategy can well learn and adapt to the dynamic nature of the travel demand and hence guarantee the robustness of the traffic dynamics.

To close the discussion, the numerical results indicate that the proposed IRL based adaptive perimeter controller can not only stabilize the network accumulation states at the desired equilibrium, but also achieve improvement in

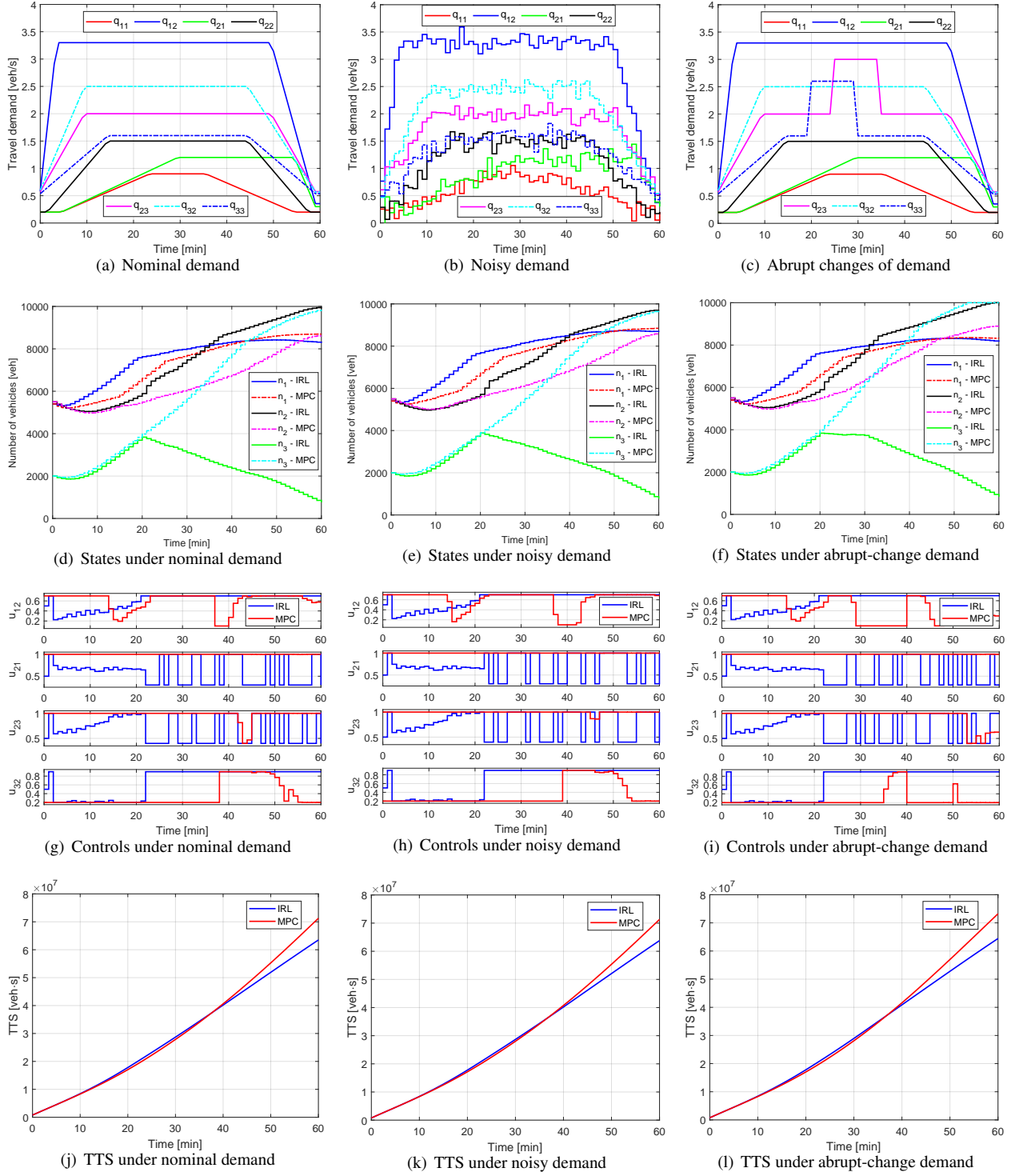


Figure 9: Simulation results of Scenario 2

min TTS compared to the state-of-the-art MPC scheme. These results demonstrate the effectiveness and efficiency of IRL under a variety of data resolutions. In addition, the proposed approach has been examined under various traffic

Table 4: Summary of TTS and computation time for Scenario 2

	nominal demand		noisy demand		abrupt-change demand	
	IRL	MPC	IRL	MPC	IRL	MPC
TTS ($\times 10^7$ veh-sec)	6.35	7.12	6.38	7.13	6.44	7.32
CPU time per step (sec)	1.07×10^{-5}	5.85×10^{-1}	1.14×10^{-5}	5.93×10^{-1}	1.24×10^{-5}	5.99×10^{-1}

conditions and demand patterns, which implies a promising application of IRL for macroscopic traffic control. The perimeter control in essence is a type of gating control actualized on the boundaries to regulate the cross-boundary traffic flows between different regions. Such kinds of perimeter control are deployed in many metropolises such as Guangzhou and Hong Kong utilizing the existing infrastructure. For example, such perimeter control has been implemented on the cross-Zhujiang-river bridges connecting two busy business districts to manage the peak-hour traffic. Similar perimeter control strategies are also implemented on existing infrastructures in Hong Kong, such as the Hung Hom Cross Harbor Tunnel connecting Hong Kong Island and Kowloon area. For a detailed discussion on the potential applications of the perimeter control, readers may refer to [Zhong et al. \(2018a,b\)](#).

7. Microscopic simulation

To further demonstrate the applicability of the proposed IRL approach to perimeter control of MFD based networks, a microscopic simulation example is presented in this section. Both training of the proposed IRL algorithm and its performance evaluation are conducted using SUMO as the environment ([Lopez et al., 2018](#)). The simulation and calculation are implemented in Python 3.6 and MATLAB R2022a.

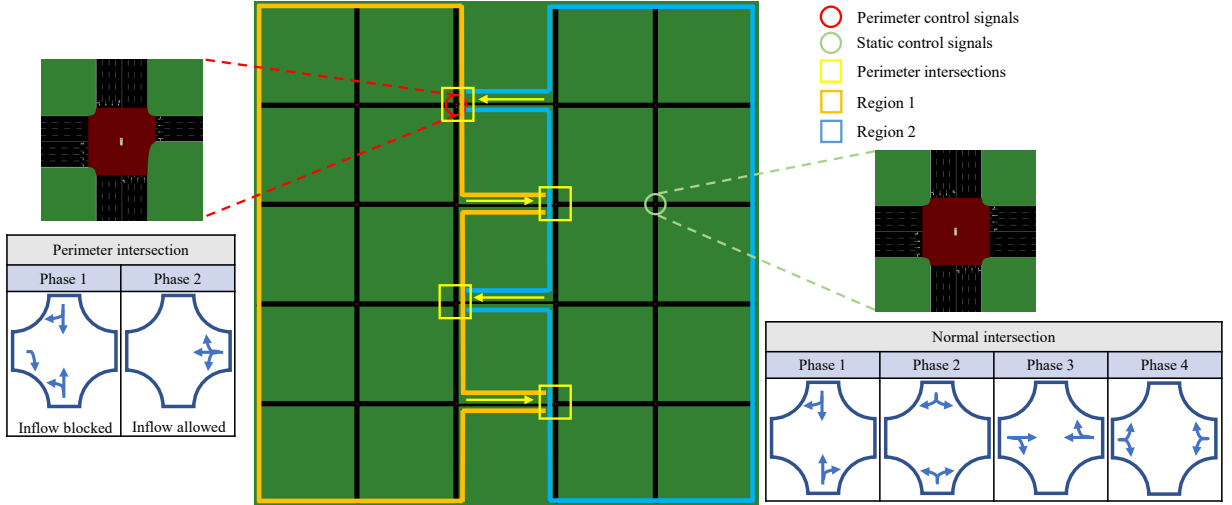


Figure 10: The simulated grid network

The microscopic simulation is carried out using a grid road network as depicted in [Figure 10](#), which comprises 2 regions (regions 1 and 2 surrounded by orange lines and blue lines, respectively), 16 signalized intersections (12 normal intersections applying an identical static signal plan and 4 perimeter intersections applying the IRL based signal plans for perimeter control actuation) and 76 links. All links are 500 meters long and comprise 4 lanes. There are 4 special links connecting the two network regions as marked alongside yellow arrows. Note that these 4 links are unidirectional and that their end nodes are signalized intersections working as the perimeter controllers (as marked with yellow rectangles). For the perimeter intersections, a two-phased signal with a 120-second cycle time is adopted (see [Figure 10](#)). Both the sample time interval and the control update step are equal to the perimeter control signal cycle time. Perimeter control inputs are implemented by changing the green duration ratios of the corresponding

perimeter intersections. Let $GR_{ij}(k)$ denotes the green duration ratio of phase 2 at the k -th ($k = 1, \dots, 90$) control update step for actualizing the computed result of $u_{ij}(k)$ and $GR_{ij}(k) = u_{ij}(k)$. The calculation of the green light duration $\mathcal{G}_{ij}(k)$ of phase 2 is $\mathcal{G}_{ij}(k) = GR_{ij}(k) \cdot CT_{ij} = u_{ij}(k) \cdot CT_{ij}$ where $CT_{ij} = 120$ (sec) is the cycle time of the perimeter intersections for u_{ij} . For instance, if the computed result of a control input is 0.6, the green light duration is set as 72 seconds for the 120-second cycle. All the normal intersections have four phases and the same cycle time 100 seconds. An identical static signal plan is adopted for the normal intersections. The total simulation time is 3 hours.

The perimeter control objective in this microscopic simulation is to minimize the TTS. Both regions are initially empty at the beginning. A time-varying travel demand pattern associated with a 10% coefficient of variation to represent the stochasticity is adopted, which mimics the morning-peak traffic with congestion onset and dissolving processes (see Figure 11(a)). The accumulation evolutions are depicted in Figure 11(b). As observed from the results, by merely manipulating the green duration ratios of the four perimeter intersections, the IRL scheme can regulate the accumulation states below the critical accumulation and achieve a significant improvement over the static scheme in avoiding congestion. Figure 11(c) shows that the IRL scheme can guarantee a low TTS at around 6.81×10^6 (veh-sec), while the static scheme results in a very high TTS at around 2.14×10^7 (veh-sec). The flow-accumulation plots by the proposed IRL approach and the static scheme are shown in Figure 11(d) and Figure 11(e), respectively. One can see that the IRL scheme results in a higher maximal throughput than the static scheme, whereas observed from the simulation process, the static scheme induces severe congestion and even gridlocks in both regions. These microscopic simulation results validate the effectiveness of the proposed IRL method in optimal perimeter control for MFD based traffic networks.

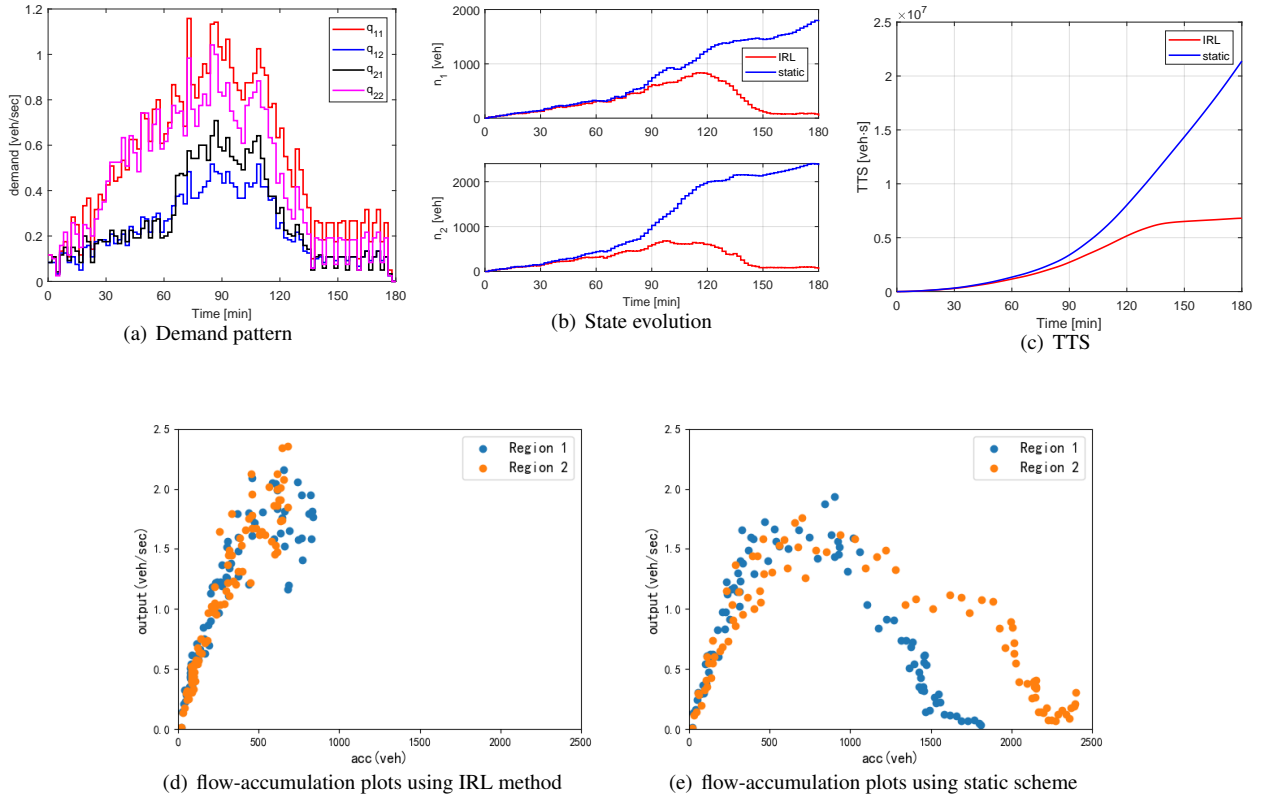


Figure 11: The microscopic simulation results

8. Conclusion

This paper developed a data-driven IRL based framework for learning macroscopic urban traffic dynamics for adaptive constrained optimal perimeter control. An online adaptive optimal perimeter control scheme with continuous-time control and discrete gain updates was established to adapt to the discrete-time nature of traffic data. To further consider the heterogeneous traffic sensors with different resolutions of data measurements, the reinforcement interval of the proposed IRL based perimeter control could be selected online to ensure data richness for the data-driven RL algorithms and allow adaptive online learning to guarantee real-time performance. An actor-critic dual neural network structure was developed to approximate the optimal control and the objective function, respectively. The actor-critic dual neural networks could be used to circumvent the “curse of dimensionality” in solving the HJB equations involved. Integrating the experience replay technique, the proposed online learning approach could adapt to the real-time traffic conditions by using the historical and real-time data simultaneously in a “smart” manner. This proposed optimal perimeter control did not explicitly employ the knowledge of traffic network dynamics, i.e., “model-free”. The convergence of learning algorithms and the stability of the traffic dynamics under control were proven via the Lyapunov theory. The proposed online iterative learning approach was tested under various traffic conditions (e.g., constant demand, time-varying demand with and without uncertainties, unknown MFD model), where the convergence, adaptiveness and robustness of the network traffic state were achieved. Both numerical examples and microscopic simulation experiments were presented to validate the applicability of the proposed method to optimal perimeter control for MFD based networks. In addition, the comparison results indicated that the proposed IRL approach could achieve both good control performance and computational efficiency.

Considering the dynamic nature of travel demand and supply, future efforts can be dedicated to investigating a novel trajectory stability concept, instead of the stability of the desired equilibrium point, to fit such dynamic travel demand and supply.

Acknowledgement

The work in this paper was jointly supported by research grants from the National Natural Science Foundation of China (No. 72071214), the National Key R&D Program of China (No. 2018YFB1600500) and the Research Grants Council of Hong Kong (Nos. R5029-18 & 15211518E).

Appendix A. Macroscopic traffic dynamics in the affine form

This appendix presents the conservation equations and dynamics in the affine form of two cases investigated in the literature, i.e., the two-region and the three-region MFD systems, as shown in Figure 4(a) and Figure 4(b), respectively. To begin with, let $M_{ii}(t) = \frac{n_{ii}(t)}{n_i(t)} G_i(n_i(t))$ and $M_{ij}(t) = \frac{n_{ij}(t)}{n_i(t)} G_i(n_i(t))$ denote the within-region flow and cross-boundary flow at time t , respectively.

Case 1: The two-region MFD system

Let $L = 2$ (i.e., the two-region MFD dynamics as shown by Figure 4(a) defined in Geroliminis et al., 2013), $n = [n_{11}, n_{12}, n_{21}, n_{22}]^T \in \mathbb{R}^4$ and $u = [u_{12}, u_{21}]^T \in \mathbb{R}^2$. The flow conservation equations are given as

$$\begin{aligned}\frac{dn_{11}(t)}{dt} &= -M_{11}(t) + M_{21}(t)u_{21}(t) + q_{11}(t) \\ \frac{dn_{12}(t)}{dt} &= -M_{12}(t)u_{12}(t) + q_{12}(t) \\ \frac{dn_{21}(t)}{dt} &= -M_{21}(t)u_{21}(t) + q_{21}(t) \\ \frac{dn_{22}(t)}{dt} &= -M_{22}(t) + M_{12}(t)u_{12}(t) + q_{22}(t)\end{aligned}$$

For this case, the new state and control are $\tilde{n} = [\tilde{n}_1, \tilde{n}_2, \tilde{n}_3, \tilde{n}_4]^T \in \mathbb{R}^4$ and $\tilde{u} = [\tilde{u}_1, \tilde{u}_2]^T \in \mathbb{R}^2$, respectively. The drift dynamics $\mathbf{F} \in \mathbb{R}^4$ and input dynamics $\mathbf{S} \in \mathbb{R}^{4 \times 2}$ of their affine-form traffic dynamics are

$$\mathbf{F}(\tilde{n}) \triangleq \begin{bmatrix} -M_{11} + M_{21}u_{21}^* + q_{11} \\ -M_{12}u_{12}^* + q_{12} \\ -M_{21}u_{21}^* + q_{21} \\ -M_{22} + M_{12}u_{12}^* + q_{22} \end{bmatrix}, \mathbf{S}(\tilde{n}) \triangleq \begin{bmatrix} 0 & M_{21} \\ -M_{12} & 0 \\ 0 & -M_{21} \\ M_{12} & 0 \end{bmatrix}$$

Case 2: The three-region MFD system

Let $L = 3$ (i.e., three-region MFD dynamics as shown by Figure 4(b), see example in Zhong et al., 2018b), $n = [n_{11}, n_{12}, n_{21}, n_{22}, n_{23}, n_{32}, n_{33}]^T \in \mathbb{R}^7$ and $u = [u_{12}, u_{21}, u_{23}, u_{32}]^T \in \mathbb{R}^4$. The flow conservation equations are given as

$$\begin{aligned} \frac{dn_{11}(t)}{dt} &= -M_{11}(t) + M_{21}(t)u_{21}(t) + q_{11}(t) \\ \frac{dn_{12}(t)}{dt} &= -M_{12}(t)u_{12}(t) + q_{12}(t) \\ \frac{dn_{21}(t)}{dt} &= -M_{21}(t)u_{21}(t) + q_{21}(t) \\ \frac{dn_{22}(t)}{dt} &= -M_{22}(t) + M_{12}(t)u_{12}(t) + M_{32}(t)u_{32}(t) + q_{22}(t) \\ \frac{dn_{23}(t)}{dt} &= -M_{23}(t)u_{23}(t) + q_{23}(t) \\ \frac{dn_{32}(t)}{dt} &= -M_{32}(t)u_{32}(t) + q_{32}(t) \\ \frac{dn_{33}(t)}{dt} &= -M_{33}(t) + M_{23}(t)u_{23}(t) + q_{33}(t) \end{aligned}$$

For this case, $\tilde{n} = [\tilde{n}_1, \dots, \tilde{n}_7]^T \in \mathbb{R}^7$ and $\tilde{u} = [\tilde{u}_1, \dots, \tilde{u}_4]^T \in \mathbb{R}^4$. $\mathbf{F} \in \mathbb{R}^7$ and $\mathbf{S} \in \mathbb{R}^{7 \times 4}$ of their affine-form traffic dynamics are

$$\mathbf{F}(\tilde{n}) \triangleq \begin{bmatrix} -M_{11} + M_{21}u_{21}^* + q_{11} \\ -M_{12}u_{12}^* + q_{12} \\ -M_{21}u_{21}^* + q_{21} \\ -M_{22} + M_{12}u_{12}^* + M_{32}u_{32}^* + q_{22} \\ -M_{23}u_{23}^* + q_{23} \\ -M_{32}u_{32}^* + q_{32} \\ -M_{33} + M_{23}u_{23}^* + q_{33} \end{bmatrix}, \mathbf{S}(\tilde{n}) \triangleq \begin{bmatrix} 0 & M_{21} & 0 & 0 \\ -M_{12} & 0 & 0 & 0 \\ 0 & -M_{21} & 0 & 0 \\ M_{12} & 0 & 0 & M_{32} \\ 0 & 0 & -M_{23} & 0 \\ 0 & 0 & 0 & -M_{32} \\ 0 & 0 & M_{23} & 0 \end{bmatrix}$$

Appendix B. Proof of Lemma 3.1

This appendix presents the proof of Lemma 3.1.

Proof. 1) Assume that V^* is the optimal value function which satisfies (19), then it yields the following HJB equation

$$\begin{aligned} H\left(\tilde{n}, \tilde{u}, \frac{\partial V^*}{\partial \tilde{n}}\right) &= \min_{\tilde{u}} \left[\mathcal{L}(\tilde{n}, \tilde{u}) + \left(\frac{\partial V^*}{\partial \tilde{n}} \right)^T (\mathbf{F}(\tilde{n}) + \mathbf{S}(\tilde{n})\tilde{u}) \right] \\ &= \min_{\tilde{u}} \left[\tilde{n}^T Q \tilde{n} + 2\tilde{v}^T R \int_{\tilde{v}}^{\tilde{u}} \tanh^{-1} \left(\frac{1}{\tilde{v}} \odot (v - \tilde{v}) \right) dv + \left(\frac{\partial V^*}{\partial \tilde{n}} \right)^T (\mathbf{F}(\tilde{n}) + \mathbf{S}(\tilde{n})\tilde{u}) \right] = 0 \\ &= \min_{\tilde{u}} \left[\tilde{n}^T Q \tilde{n} + \sum_{k_u=1}^{\alpha_u} 2\tilde{v}_{k_u} \gamma_{k_u} \int_{\tilde{v}_{k_u}}^{\tilde{u}_{k_u}} \tanh^{-1} \left(\frac{v_{k_u} - \tilde{v}_{k_u}}{\tilde{v}_{k_u}} \right) dv_{k_u} + \left(\frac{\partial V^*}{\partial \tilde{n}} \right)^T \mathbf{F}(\tilde{n}) + \sum_{k_u=1}^{\alpha_u} \sum_{k_n=1}^{\alpha_n} \frac{\partial V^*}{\partial \tilde{n}_{k_n}} S_{k_n, k_u} \tilde{u}_{k_u} \right] \quad (\text{B.1}) \end{aligned}$$

where S_{k_n, k_u} denotes the k_n -th element of the k_u -th column of \mathbf{S} .

The optimal constrained perimeter control $\tilde{u}_{k_u}^*$ is calculated by applying the stationary (optimal) condition $\partial H / \partial \tilde{u}_{k_u}^* = 0$, i.e.,

$$\frac{\partial H}{\partial \tilde{u}_{k_u}^*} = 2\underline{v}_{k_u} \gamma_{k_u} \tanh^{-1} \left(\frac{\tilde{u}_{k_u}^* - \bar{v}_{k_u}}{\underline{v}_{k_u}} \right) + \sum_{k_n=1}^{\alpha_n} \frac{\partial V^*}{\partial \tilde{n}_{k_n}} S_{k_n, k_u} = 0$$

Then it follows that

$$\begin{aligned} \tanh^{-1} \left(\frac{\tilde{u}_{k_u}^* - \bar{v}_{k_u}}{\underline{v}_{k_u}} \right) &= -\frac{1}{2\underline{v}_{k_u} \gamma_{k_u}} \sum_{k_n=1}^{\alpha_n} \frac{\partial V^*}{\partial \tilde{n}_{k_n}} S_{k_n, k_u} \\ \Rightarrow \frac{\tilde{u}_{k_u}^* - \bar{v}_{k_u}}{\underline{v}_{k_u}} &= \tanh \left(-\frac{1}{2\underline{v}_{k_u} \gamma_{k_u}} \sum_{k_n=1}^{\alpha_n} \frac{\partial V^*}{\partial \tilde{n}_{k_n}} S_{k_n, k_u} \right) = -\tanh \left(\frac{1}{2\underline{v}_{k_u} \gamma_{k_u}} \sum_{k_n=1}^{\alpha_n} \frac{\partial V^*}{\partial \tilde{n}_{k_n}} S_{k_n, k_u} \right) \\ \Rightarrow \tilde{u}_{k_u}^* &= -\underline{v}_{k_u} \tanh \left(\frac{1}{2\underline{v}_{k_u} \gamma_{k_u}} \sum_{k_n=1}^{\alpha_n} \frac{\partial V^*}{\partial \tilde{n}_{k_n}} S_{k_n, k_u} \right) + \bar{v}_{k_u} \end{aligned}$$

Let $D_{k_u}^* = \frac{1}{2\underline{v}_{k_u} \gamma_{k_u}} \sum_{k_n=1}^{\alpha_n} \frac{\partial V^*}{\partial \tilde{n}_{k_n}} S_{k_n, k_u}$ be the k_u -th unconstrained optimal control input. The optimal control $\tilde{u}_{k_u}^*$ is obtained as

$$\tilde{u}_{k_u}^* = -\underline{v}_{k_u} \tanh(D_{k_u}^*) + \bar{v}_{k_u} \quad (\text{B.2})$$

Therefore, the constrained optimal perimeter control is given by

$$\tilde{u}^* = -\underline{v} \odot \tanh(D^*) + \bar{v}, \text{ with } D^* = \frac{1}{2\underline{v}} \odot \left(R^{-1} \mathbf{S}^T \frac{\partial V^*}{\partial \tilde{n}} \right) \quad (\text{B.3})$$

2) Let $\hat{v} = \frac{1}{\underline{v}} \odot (v - \bar{v})$. Substituting (B.3) into (17), we have

$$\begin{aligned} U(\tilde{u}^*) &= 2\underline{v}^T \odot \underline{v}^T R \int_0^{\frac{1}{\underline{v}} \odot (\tilde{u}^* - \bar{v})} \tanh^{-1}(\hat{v}) d\hat{v} = 2\underline{v}^T R \int_0^{-\tanh(D^*)} \tanh^{-1}(\hat{v}) d\hat{v} \\ &= 2\underline{v}^T R \cdot \left(\hat{v} \odot \tanh^{-1}(\hat{v}) + \frac{1}{2} \ln(\mathbf{1}_{\alpha_u} - \hat{v}^2) \right) \Big|_0^{-\tanh(D^*)} = 2\underline{v}^T R \left(\tanh(D^*) \odot D^* + \frac{1}{2} \ln(\mathbf{1}_{\alpha_u} - \tanh^2(D^*)) \right) \\ &= 2\underline{v}^T R (D^* \odot \tanh(D^*)) + \underline{v}^T R \ln(\mathbf{1}_{\alpha_u} - \tanh^2(D^*)) \\ &= 2\underline{v}^T R \left(\frac{1}{2\underline{v}} \odot \left(R^{-1} \mathbf{S}^T \frac{\partial V^*}{\partial \tilde{n}} \right) \odot \tanh(D^*) \right) + \underline{v}^T R \ln(\mathbf{1}_{\alpha_u} - \tanh^2(D^*)) \\ &= \left(\frac{\partial V^*}{\partial \tilde{n}} \right)^T \mathbf{S}(\tilde{n}) (\underline{v} \odot \tanh(D^*)) + \underline{v}^T R \ln(\mathbf{1}_{\alpha_u} - \tanh^2(D^*)) \end{aligned} \quad (\text{B.4})$$

Then substituting (B.3)-(B.4) into (B.1), the HJB equation can further be expressed by

$$\begin{aligned} 0 &= \tilde{n}^T Q \tilde{n} + \left(\frac{\partial V^*}{\partial \tilde{n}} \right)^T (\mathbf{F} + \mathbf{S} \tilde{u}^*) + \left(\frac{\partial V^*}{\partial \tilde{n}} \right)^T \mathbf{S} (\underline{v} \odot \tanh(D^*)) + \underline{v}^T R \ln(\mathbf{1}_{\alpha_u} - \tanh^2(D^*)) \\ &= \tilde{n}^T Q \tilde{n} + \left(\frac{\partial V^*}{\partial \tilde{n}} \right)^T \mathbf{F} + \left(\frac{\partial V^*}{\partial \tilde{n}} \right)^T \mathbf{S} \tilde{u}^* + \left(\frac{\partial V^*}{\partial \tilde{n}} \right)^T \mathbf{S} \cdot (\underline{v} \odot \tanh(D^*)) + \underline{v}^T R \ln(\mathbf{1}_{\alpha_u} - \tanh^2(D^*)) \\ &= \tilde{n}^T Q \tilde{n} + \left(\frac{\partial V^*}{\partial \tilde{n}} \right)^T \mathbf{F} + \left(\frac{\partial V^*}{\partial \tilde{n}} \right)^T \mathbf{S} \cdot (-\underline{v} \odot \tanh(D^*) + \bar{v}) + \left(\frac{\partial V^*}{\partial \tilde{n}} \right)^T \mathbf{S} \cdot (\underline{v} \odot \tanh(D^*)) + \underline{v}^T R \ln(\mathbf{1}_{\alpha_u} - \tanh^2(D^*)) \\ &= \tilde{n}^T Q \tilde{n} + \left(\frac{\partial V^*}{\partial \tilde{n}} \right)^T \mathbf{F} + \left(\frac{\partial V^*}{\partial \tilde{n}} \right)^T \mathbf{S} \bar{v} + \underline{v}^T R \ln(\mathbf{1}_{\alpha_u} - \tanh^2(D^*)) \end{aligned} \quad (\text{B.5})$$

That is, if (V^*, D^*) is the solution to the COPCP, (V^*, D^*) should satisfy (B.5). This completes the proof. \blacksquare \square

Appendix C. Proof of Lemma 4.1

This appendix presents the proof of Lemma 4.1. To prove this lemma, we need the following Lemma Appendix C.1.

Lemma Appendix C.1. For a monotonically increasing odd function $\varrho(x)$, we have

- 1) $\varrho(x) \cdot (y - x) - \int_x^y \varrho(s)ds \leq 0, \forall x, y;$
- 2) $\varrho(x) \cdot (y - x) - \int_0^y \varrho(s)ds \leq 0, \forall x, y.$

■

Proof. 1) Without loss of generality, we assume that $y \geq x$.

Note that $\varrho(x)$ is monotonically increasing and odd. Thus,

$$\varrho(x) \begin{cases} < 0, & x < 0 \\ = 0, & x = 0 \\ > 0, & x > 0 \end{cases}, \varrho(-x) = -\varrho(x)$$

Then we have $\int_x^y \varrho(s)ds \geq 0$. Moreover, $\int_x^y \varrho(s)ds = 0$ if and only if $y = x$.

Let $\varphi(y) = \varrho(x) \cdot (y - x) - \int_x^y \varrho(s)ds$, then

$$\frac{d\varphi}{dy} = \varrho(x) - \varrho(y) \begin{cases} > 0, & y < x \\ = 0, & y = x \\ < 0, & y > x \end{cases}$$

The extreme value of $\varphi(y)$ is obtained at $y = x$, i.e., $\varphi(x) = 0 - \int_x^x \varrho(s)ds \leq 0$. $\varphi(y) = 0$ if and only if $y = x$. Thus, we have

$$\varrho(x) \cdot (y - x) - \int_x^y \varrho(s)ds \leq 0$$

and $\varrho(x) \cdot (y - x) - \int_x^y \varrho(s)ds = 0$ if and only if $y = x$.

2) The left side of the second part of Lemma Appendix C.1 can be written as

$$\varrho(x) \cdot (y - x) - \int_0^y \varrho(s)ds = \varrho(x) \cdot (y - 0) - \int_0^y \varrho(s)ds - \varrho(x)x \quad (C.1)$$

Based on the first part, we have $\varrho(x) \cdot (y - 0) - \int_0^y \varrho(s)ds \leq 0$. Because $\varrho(x)$ and x are monotonically increasing and odd, one has $\varrho(x)x \geq 0$, i.e., $-\varrho(x)x \leq 0$. Thus, we have

$$\varrho(x) \cdot (y - x) - \int_0^y \varrho(s)ds \leq 0$$

Moreover, $\varrho(x) \cdot (y - x) - \int_0^y \varrho(s)ds = 0$ if and only if $y = x = 0$. This completes the proof. ■

□

Now we present the proof of Lemma 4.1.

Proof. 1) Taking the derivative of V^{k+1} along the system $\mathbf{F} + \mathbf{S}\tilde{\mathbf{u}}^{k+1}$ trajectory, we have

$$\dot{V}^{k+1} = \left(\frac{\partial V^{k+1}}{\partial \tilde{\mathbf{n}}} \right)^T \mathbf{F} + \left(\frac{\partial V^{k+1}}{\partial \tilde{\mathbf{n}}} \right)^T \mathbf{S}\tilde{\mathbf{u}}^{k+1} \quad (C.2)$$

Based on (18) and (25), we have

$$\begin{aligned} & N(\tilde{n}) + 2\underline{v}^T R \int_{\bar{v}}^{\tilde{u}^k} \tanh^{-1}\left(\frac{1}{\underline{v}} \odot (v - \bar{v})\right) dv + \left(\frac{\partial V^{k+1}}{\partial \tilde{n}}\right)^T \mathbf{F} + \left(\frac{\partial V^{k+1}}{\partial \tilde{n}}\right)^T \mathbf{S} \tilde{u}^k = 0 \\ \Rightarrow & \left(\frac{\partial V^{k+1}}{\partial \tilde{n}}\right)^T \mathbf{F} = -\left(\frac{\partial V^{k+1}}{\partial \tilde{n}}\right)^T \mathbf{S} \tilde{u}^k - N(\tilde{n}) - 2\underline{v}^T R \int_{\bar{v}}^{\tilde{u}^k} \tanh^{-1}\left(\frac{1}{\underline{v}} \odot (v - \bar{v})\right) dv \end{aligned} \quad (\text{C.3})$$

From (26), one has

$$\begin{aligned} & \tilde{u}^{k+1} - \bar{v} = -\underline{v} \odot \tanh\left(\frac{1}{2\underline{v}} \odot \left(R^{-1} \mathbf{S}^T \frac{\partial V^{k+1}}{\partial \tilde{n}}\right)\right) \\ \Rightarrow & \frac{1}{\underline{v}} \odot (\tilde{u}^{k+1} - \bar{v}) = -\tanh\left(\frac{1}{2\underline{v}} \odot \left(R^{-1} \mathbf{S}^T \frac{\partial V^{k+1}}{\partial \tilde{n}}\right)\right) \\ \Rightarrow & \tanh^{-1}\left(\frac{1}{\underline{v}} \odot (\tilde{u}^{k+1} - \bar{v})\right) = -\frac{1}{2\underline{v}} \odot \left(R^{-1} \mathbf{S}^T \frac{\partial V^{k+1}}{\partial \tilde{n}}\right) \\ \Rightarrow & -2\underline{v} \odot \tanh^{-1}\left(\frac{1}{\underline{v}} \odot (\tilde{u}^{k+1} - \bar{v})\right) = R^{-1} \mathbf{S}^T \frac{\partial V^{k+1}}{\partial \tilde{n}} \\ \Rightarrow & \left(\frac{\partial V^{k+1}}{\partial \tilde{n}}\right)^T \mathbf{S} = -2\underline{v}^T \odot \tanh^{-T}\left(\frac{1}{\underline{v}} \odot (\tilde{u}^{k+1} - \bar{v})\right) R \end{aligned} \quad (\text{C.4})$$

Substitute (C.3)-(C.4) into (C.2), it follows that

$$\begin{aligned} \dot{V}^{k+1} &= -N(\tilde{n}) - 2\underline{v}^T R \int_{\bar{v}}^{\tilde{u}^k} \tanh^{-1}\left(\frac{1}{\underline{v}} \odot (v - \bar{v})\right) dv - \left(\frac{\partial V^{k+1}}{\partial \tilde{n}}\right)^T \mathbf{S} \tilde{u}^k - 2\underline{v}^T \odot \tanh^{-T}\left(\frac{1}{\underline{v}} \odot (\tilde{u}^{k+1} - \bar{v})\right) R \tilde{u}^{k+1} \\ &= -N(\tilde{n}) - 2\underline{v}^T R \int_{\bar{v}}^{\tilde{u}^k} \tanh^{-1}\left(\frac{1}{\underline{v}} \odot (v - \bar{v})\right) dv + 2\underline{v}^T \odot \tanh^{-T}\left(\frac{1}{\underline{v}} \odot (\tilde{u}^{k+1} - \bar{v})\right) R \tilde{u}^k - 2\underline{v}^T \odot \tanh^{-T}\left(\frac{1}{\underline{v}} \odot (\tilde{u}^{k+1} - \bar{v})\right) R \tilde{u}^{k+1} \\ &= -N(\tilde{n}) - 2\left(\underline{v}^T R \int_{\bar{v}}^{\tilde{u}^k} \tanh^{-1}\left(\frac{1}{\underline{v}} \odot (v - \bar{v})\right) dv - \underline{v}^T \odot \tanh^{-T}\left(\frac{1}{\underline{v}} \odot (\tilde{u}^{k+1} - \bar{v})\right) R \tilde{u}^k + \underline{v}^T \odot \tanh^{-T}\left(\frac{1}{\underline{v}} \odot (\tilde{u}^{k+1} - \bar{v})\right) R \tilde{u}^{k+1}\right) \\ &= -N(\tilde{n}) + 2\left(\underline{v}^T \odot \tanh^{-T}\left(\frac{1}{\underline{v}} \odot (\tilde{u}^{k+1} - \bar{v})\right) R (\tilde{u}^k - \tilde{u}^{k+1}) - \underline{v}^T R \int_{\bar{v}}^{\tilde{u}^k} \tanh^{-1}\left(\frac{1}{\underline{v}} \odot (v - \bar{v})\right) dv\right) \\ &= -N(\tilde{n}) + 2\left(\sum_{k_u=1}^{\alpha_u} \underline{v}_{k_u} \gamma_{k_u} \tanh^{-1}\left(\frac{\tilde{u}_{k_u}^{k+1} - \bar{v}_{k_u}}{\underline{v}_{k_u}}\right) (\tilde{u}_{k_u}^k - \tilde{u}_{k_u}^{k+1}) - \sum_{k_u=1}^{\alpha_u} \underline{v}_{k_u} \gamma_{k_u} \int_{\bar{v}_{k_u}}^{\tilde{u}_{k_u}^k} \tanh^{-1}\left(\frac{v_{k_u} - \bar{v}_{k_u}}{\underline{v}_{k_u}}\right) dv_{k_u}\right) \\ &= -N(\tilde{n}) + 2\sum_{k_u=1}^{\alpha_u} \underline{v}_{k_u} \gamma_{k_u} \left(\tanh^{-1}\left(\frac{\tilde{u}_{k_u}^{k+1} - \bar{v}_{k_u}}{\underline{v}_{k_u}}\right) (\tilde{u}_{k_u}^k - \tilde{u}_{k_u}^{k+1}) - \int_{\bar{v}_{k_u}}^{\tilde{u}_{k_u}^k} \tanh^{-1}\left(\frac{v_{k_u} - \bar{v}_{k_u}}{\underline{v}_{k_u}}\right) dv_{k_u}\right) \end{aligned} \quad (\text{C.5})$$

Let $\varrho(x) \triangleq \tanh^{-1}(x/\underline{v}_{k_u})$ for $\forall x \in \mathbb{R}$, $s_{k_u}^k = \tilde{u}_{k_u}^k - \bar{v}_{k_u}$ and $\hat{v}_{k_u} = v_{k_u} - \bar{v}_{k_u}$. Then (C.5) is rewritten as follows

$$\dot{V}^{k+1} = -N(\tilde{n}) + 2\sum_{k_u=1}^{\alpha_u} \underline{v}_{k_u} \gamma_{k_u} \left(\varrho(s_{k_u}^{k+1})(s_{k_u}^k - s_{k_u}^{k+1}) - \int_0^{s_{k_u}^k} \varrho(\hat{v}_{k_u}) d\hat{v}_{k_u}\right)$$

Since $\tanh^{-1}(\cdot)$ is a monotonically increasing odd function, $\varrho(x)$ is monotonically increasing and odd. By Lemma Appendix C.1, the following inequality holds

$$\varrho(s_{k_u}^{k+1})(s_{k_u}^k - s_{k_u}^{k+1}) - \int_0^{s_{k_u}^k} \varrho(\hat{v}_{k_u}) d\hat{v}_{k_u} \leq 0$$

Recall that $\underline{v} > 0$ and $\gamma > 0$, we have $\dot{V}^{k+1} \leq 0$ and $V^{k+1}(\tilde{n})$ is a Lyapunov function for \tilde{u}^{k+1} on Ω .

Because the nonlinear function \mathbf{S} is continuous and $V^{k+1}(0) = 0$, $\tilde{u}^{k+1}(\tilde{n}) \in C^1(\Omega)$ and $\tilde{u}^{k+1}(0) = 0$, i.e., the obtained control policies $\tilde{u}^{k+1}(\tilde{n})$ in (26) are admissible as per Definition 2.1 for system (14) on Ω .

2) First, we prove that $V^{k+2}(\tilde{n}(t)) \leq V^{k+1}(\tilde{n}(t))$.

Considering $V(\tilde{n})$ defined in (18) along the system $\mathbf{F} + \mathbf{S}\tilde{u}^{k+1}$ trajectory, we have

$$V^{k+2}(\tilde{n}) - V^{k+1}(\tilde{n}) = - \int_t^\infty \left(\frac{\partial(V^{k+2} - V^{k+1})^T}{\partial \tilde{n}} (\mathbf{F} + \mathbf{S}\tilde{u}^{k+1}) \right) d\tau \quad (\text{C.6})$$

Since $(V^{k+1}(\tilde{n}), \tilde{u}^k(\tilde{n}))$ and $(V^{k+2}(\tilde{n}), \tilde{u}^{k+1}(\tilde{n}))$ both satisfy (19), we can obtain

$$\left(\frac{\partial V^{k+1}}{\partial \tilde{n}} \right)^T \mathbf{F} = -N(\tilde{n}) - 2\underline{v}^T R \int_{\underline{v}}^{\tilde{u}^k} \tanh^{-1} \left(\frac{1}{\underline{v}} \odot (\nu - \bar{\nu}) \right) d\nu - \left(\frac{\partial V^{k+1}}{\partial \tilde{n}} \right)^T \mathbf{S}\tilde{u}^k \quad (\text{C.7a})$$

$$\left(\frac{\partial V^{k+2}}{\partial \tilde{n}} \right)^T \mathbf{F} = -N(\tilde{n}) - 2\underline{v}^T R \int_{\underline{v}}^{\tilde{u}^{k+1}} \tanh^{-1} \left(\frac{1}{\underline{v}} \odot (\nu - \bar{\nu}) \right) d\nu - \left(\frac{\partial V^{k+2}}{\partial \tilde{n}} \right)^T \mathbf{S}\tilde{u}^{k+1} \quad (\text{C.7b})$$

Substituting (C.7a)-(C.7b) into (C.6), we get

$$\begin{aligned} V^{k+2}(\tilde{n}) - V^{k+1}(\tilde{n}) &= - \int_t^\infty \left(\left(\frac{\partial V^{k+2}}{\partial \tilde{n}} \right)^T \mathbf{F} - \left(\frac{\partial V^{k+1}}{\partial \tilde{n}} \right)^T \mathbf{F} + \left(\frac{\partial V^{k+2}}{\partial \tilde{n}} \right)^T \mathbf{S}\tilde{u}^{k+1} - \left(\frac{\partial V^{k+1}}{\partial \tilde{n}} \right)^T \mathbf{S}\tilde{u}^{k+1} \right) d\tau \\ &= - \int_t^\infty \left(-N(\tilde{n}) - 2\underline{v}^T R \int_{\underline{v}}^{\tilde{u}^{k+1}} \tanh^{-1} \left(\frac{1}{\underline{v}} \odot (\nu - \bar{\nu}) \right) d\nu - \left(\frac{\partial V^{k+2}}{\partial \tilde{n}} \right)^T \mathbf{S}\tilde{u}^{k+1} \right. \\ &\quad \left. + N(\tilde{n}) + 2\underline{v}^T R \int_{\underline{v}}^{\tilde{u}^k} \tanh^{-1} \left(\frac{1}{\underline{v}} \odot (\nu - \bar{\nu}) \right) d\nu + \left(\frac{\partial V^{k+1}}{\partial \tilde{n}} \right)^T \mathbf{S}\tilde{u}^k \right. \\ &\quad \left. + \left(\frac{\partial V^{k+2}}{\partial \tilde{n}} \right)^T \mathbf{S}\tilde{u}^{k+1} - \left(\frac{\partial V^{k+1}}{\partial \tilde{n}} \right)^T \mathbf{S}\tilde{u}^{k+1} \right) d\tau \\ &= - \int_t^\infty \left(2\underline{v}^T R \int_{\tilde{u}^{k+1}}^{\tilde{u}^k} \tanh^{-1} \left(\frac{1}{\underline{v}} \odot (\nu - \bar{\nu}) \right) d\nu + \left(\frac{\partial V^{k+1}}{\partial \tilde{n}} \right)^T \mathbf{S}(\tilde{u}^k - \tilde{u}^{k+1}) \right) d\tau \end{aligned} \quad (\text{C.8})$$

Substituting (C.4) into (C.8), one obtains

$$\begin{aligned} V^{k+2}(\tilde{n}) - V^{k+1}(\tilde{n}) &= - \int_t^\infty \left(2\underline{v}^T R \int_{\tilde{u}^{k+1}}^{\tilde{u}^k} \tanh^{-1} \left(\frac{1}{\underline{v}} \odot (\nu - \bar{\nu}) \right) d\nu - 2\underline{v}^T \odot \tanh^{-T} \left(\frac{1}{\underline{v}} \odot (\tilde{u}^{k+1} - \bar{\nu}) \right) R(\tilde{u}^k - \tilde{u}^{k+1}) \right) d\tau \\ &= 2 \int_t^\infty \left(\underline{v}^T \odot \tanh^{-T} \left(\frac{1}{\underline{v}} \odot (\tilde{u}^{k+1} - \bar{\nu}) \right) R(\tilde{u}^k - \tilde{u}^{k+1}) - \underline{v}^T R \int_{\tilde{u}^{k+1}}^{\tilde{u}^k} \tanh^{-1} \left(\frac{1}{\underline{v}} \odot (\nu - \bar{\nu}) \right) d\nu \right) d\tau \\ &= 2 \int_t^\infty \left(\sum_{k_u=1}^{\alpha_u} \underline{v}_{k_u} \gamma_{k_u} \tanh^{-1} \left(\frac{\tilde{u}_{k_u}^{k+1} - \bar{v}_{k_u}}{\underline{v}_{k_u}} \right) (\tilde{u}_{k_u}^k - \tilde{u}_{k_u}^{k+1}) - \sum_{k_u=1}^{\alpha_u} \underline{v}_{k_u} \gamma_{k_u} \int_{\tilde{u}_{k_u}^{k+1}}^{\tilde{u}_{k_u}^k} \tanh^{-1} \left(\frac{v_{k_u} - \bar{v}_{k_u}}{\underline{v}_{k_u}} \right) dv_{k_u} \right) d\tau \\ &= 2 \sum_{k_u=1}^{\alpha_u} \underline{v}_{k_u} \gamma_{k_u} \int_t^\infty \left(\tanh^{-1} \left(\frac{\tilde{u}_{k_u}^{k+1} - \bar{v}_{k_u}}{\underline{v}_{k_u}} \right) (\tilde{u}_{k_u}^k - \tilde{u}_{k_u}^{k+1}) - \int_{\tilde{u}_{k_u}^{k+1}}^{\tilde{u}_{k_u}^k} \tanh^{-1} \left(\frac{v_{k_u} - \bar{v}_{k_u}}{\underline{v}_{k_u}} \right) dv_{k_u} \right) d\tau \\ &= 2 \sum_{k_u=1}^{\alpha_u} \underline{v}_{k_u} \gamma_{k_u} \int_t^\infty \left(\varrho(s_{k_u}^{k+1})(s_{k_u}^k - s_{k_u}^{k+1}) - \int_{s_{k_u}^{k+1}}^{s_{k_u}^k} \varrho(\hat{v}_{k_u}) d\hat{v}_{k_u} \right) d\tau \end{aligned} \quad (\text{C.9})$$

By Lemma Appendix C.1, the following inequality holds

$$\varrho(s_{k_u}^{k+1})(s_{k_u}^k - s_{k_u}^{k+1}) - \int_{s_{k_u}^{k+1}}^{s_{k_u}^k} \varrho(\hat{v}_{k_u}) d\hat{v}_{k_u} \leq 0$$

Thus, the right side of (C.9) is negative semi-definite. It follows that $V^{k+2}(\tilde{n}) - V^{k+1}(\tilde{n}) \leq 0$, i.e., $V^{k+2}(\tilde{n}) \leq V^{k+1}(\tilde{n})$.

Next, we prove that $V^*(\tilde{n}) \leq V^{k+2}(\tilde{n})$.

Since (V^*, \tilde{u}^*) , which satisfies (19), is the optimal solution to the COPCP defined by (14)-(15), for $\forall \tilde{n} \in \Omega$, we have $\min_{\tilde{u}} V(\tilde{n}) = V^*(\tilde{n})$ and $\tilde{u}^* = \arg \min_{\tilde{u}} \int_t^\infty \mathcal{L}(\tilde{n}(\tau), \tilde{u}(\tau)) d\tau = \arg \min_{\tilde{u}} V(\tilde{n}(t))$.

Suppose $\exists k$ such that $V^{k+2}(\tilde{n})$, which also satisfies (19), is smaller than $V^*(\tilde{n})$, i.e., $V^{k+2}(\tilde{n}) < V^*(\tilde{n})$. This means that $V^*(\tilde{n})$ is not the optimal solution to the COPCP. By contradiction, we can deduce that $V^*(\tilde{n}) \leq V^{k+2}(\tilde{n})$.

3) It follows from the second part of Lemma 4.1 that $\{V^k\}_{k=0}^\infty$ is a monotonically decreasing sequence with the lower bounded $V^*(\tilde{n})$, then V^k converges pointwise to V^* . Because of the uniqueness of $V(\tilde{n})$ with $\tilde{n} \in \Omega$ (Lewis et al., 2012; Lyashevskiy, 1996), we can get that $V^\infty = V^*$, which means that $\lim_{k \rightarrow \infty} V^k(\tilde{n}) = V^*(\tilde{n})$.

4) Since $\lim_{k \rightarrow \infty} V^k(\tilde{n}) = V^*(\tilde{n})$, according to (26), it can be deduced that $\lim_{k \rightarrow \infty} \tilde{u}^k(\tilde{n}) = \tilde{u}^*(\tilde{n})$. The proof is completed. ■

References

- Aalipour, A., Kebriaei, H., and Ramezani, M., 2018. Analytical optimal solution of perimeter traffic flow control based on mfd dynamics: A pontryagin's maximum principle approach. *IEEE Trans. Intell. Transp. Syst.*
- Aboudolas, K. and Geroliminis, N., 2013. Perimeter and boundary flow control in multi-reservoir heterogeneous networks. *Transp. Res. Part B: Methodol.*, 55:265–281.
- Abu-Khalaf, M. and Lewis, F. L., 2005. Nearly optimal control laws for nonlinear systems with saturating actuators using a neural network hjb approach. *Automatica*, 41(5):779–791.
- Abu-Khalaf, M., Huang, J., and Lewis, F. L., 2006. *Nonlinear H2/H-Infinity Constrained Feedback Control: A Practical Design Approach Using Neural Networks*. Springer Science & Business Media.
- Abu-Khalaf, M., Lewis, F. L., and Huang, J., 2008. Neurodynamic programming and zero-sum games for constrained control systems. *IEEE Transactions on Neural Networks*, 19(7):1243–1252.
- Baldi, S., Michailidis, I., Ntampasi, V., Kosmatopoulos, E., Papamichail, I., and Papageorgiou, M., 2019. A simulation-based traffic signal control for congested urban traffic networks. *Transportation Science*, 53(1):6–20.
- Daganzo, C. F., 2007. Urban gridlock: Macroscopic modeling and mitigation approaches. *Transp. Res. Part B: Methodol.*, 41(1):49–62.
- Daganzo, C. F. and Geroliminis, N., 2008. An analytical approximation for the macroscopic fundamental diagram of urban traffic. *Transp. Res. Part B: Methodol.*, 42(9):771–781.
- Daganzo, C. F., Gayah, V. V., and Gonzales, E. J., 2011. Macroscopic relations of urban traffic variables: Bifurcations, multivaluedness and instability. *Transp. Res. Part B: Methodol.*, 45(1):278–288.
- Ding, H., Zhou, J., Zheng, X., Zhu, L., Bai, H., and Zhang, W., 2020. Perimeter control for congested areas of a large-scale traffic network: A method against state degradation risk. *Transp. Res. Part C*, 112:28–45.
- Franklin, G. F., Powell, J. D., and Emami-Naeini, A., 2015. *Feedback control of dynamic systems*. Pearson London.
- Fu, H., Liu, N., and Hu, G., 2017. Hierarchical perimeter control with guaranteed stability for dynamically coupled heterogeneous urban traffic. *Transp. Res. Part C*, 83:18–38.
- Gartner, N. H. and Wagner, P., 2004. Analysis of traffic flow characteristics on signalized arterials. *Transp. Res. Rec.*, 1883(1):94–100.
- Gayah, V. V. and Daganzo, C. F., 2011. Clockwise hysteresis loops in the macroscopic fundamental diagram: an effect of network instability. *Transp. Res. Part B: Methodol.*, 45(4):643–655.
- Gayah, V. V., Gao, X. S., and Nagle, A. S., 2014. On the impacts of locally adaptive signal control on urban network stability and the macroscopic fundamental diagram. *Transp. Res. Part B: Methodol.*, 70:255–268.
- Geroliminis, N. and Boyacı, B., 2012. The effect of variability of urban systems characteristics in the network capacity. *Transp. Res. Part B: Methodol.*, 46(10):1607–1623.
- Geroliminis, N. and Daganzo, C. F., 2008. Existence of urban-scale macroscopic fundamental diagrams: Some experimental findings. *Transp. Res. Part B: Methodol.*, 42(9):759–770.
- Geroliminis, N., Haddad, J., and Ramezani, M., 2013. Optimal perimeter control for two urban regions with macroscopic fundamental diagrams: A model predictive approach. *IEEE Trans. Intell. Transp. Syst.*, 14(1):348–359.
- Godfrey, J., 1969. The mechanism of a road network. *Traffic Engineering & Control*, 8(8).
- Haddad, J., 2015. Robust constrained control of uncertain macroscopic fundamental diagram networks. *Transp. Res. Part C*, (59):323–339.
- Haddad, J., 2017a. Optimal coupled and decoupled perimeter control in one-region cities. *Control Engineering Practice*, 61:134–148.
- Haddad, J., 2017b. Optimal perimeter control synthesis for two urban regions with aggregate boundary queue dynamics. *Transp. Res. Part B: Methodol.*, 96:1–25.
- Haddad, J. and Geroliminis, N., 2012. On the stability of traffic perimeter control in two-region urban cities. *Transp. Res. Part B: Methodol.*, 46(9):1159–1176.
- Haddad, J. and Mirkin, B., 2016. Adaptive perimeter traffic control of urban road networks based on MFD model with time delays. *International Journal of Robust and Nonlinear Control*, 26(6):1267–1285.
- Haddad, J. and Shraiber, A., 2014. Robust perimeter control design for an urban region. *Transp. Res. Part B: Methodol.*, 68:315–332.
- Haddad, J. and Zheng, Z., 2020. Adaptive perimeter control for multi-region accumulation-based models with state delays. *Transp. Res. Part B: Methodol.*, 137:133–153.
- Haddad, J., Ramezani, M., and Geroliminis, N., 2013. Cooperative traffic control of a mixed network with two urban regions and a freeway. *Transp. Res. Part B: Methodol.*, 54:17–36.
- Helbing, D., 2009. Derivation of a fundamental diagram for urban traffic flow. *The European Physical Journal B*, 70(2):229–241.

- Hunt, P., Robertson, D., Bretherton, R., and Royle, M. C., 1982. The scoot on-line traffic signal optimisation technique. *Traffic Engineering & Control*, 23(4).
- Ji, Y. and Geroliminis, N., 2012. On the spatial partitioning of urban transportation networks. *Transp. Res. Part B: Methodol.*, 46(10):1639–1656.
- Ji, Y., Daamen, W., Hoogendoorn, S., Hoogendoorn-Lanser, S., and Qian, X., 2010. Investigating the shape of the macroscopic fundamental diagram using simulation data. *Transp. Res. Rec.*, 2161(1):40–48.
- Keyvan-Ekbatani, M., Kouvelas, A., Papamichail, I., and Papageorgiou, M., 2012. Exploiting the fundamental diagram of urban networks for feedback-based gating. *Transp. Res. Part B: Methodol.*, 46(10):1393–1403.
- Keyvan-Ekbatani, M., Papageorgiou, M., and Papamichail, I., 2013. Urban congestion gating control based on reduced operational network fundamental diagrams. *Transp. Res. Part C*, 33:74–87.
- Keyvan-Ekbatani, M., Papageorgiou, M., and Knoop, V. L., 2015a. Controller design for gating traffic control in presence of time-delay in urban road networks. *Transportation Research Procedia*, 7:651–668.
- Keyvan-Ekbatani, M., Yildirimoglu, M., Geroliminis, N., and Papageorgiou, M., 2015b. Multiple concentric gating traffic control in large-scale urban networks. *IEEE Trans. Intell. Transp. Syst.*, 16(4):2141–2154.
- Kheterpal, N., Parvate, K., Wu, C., Kreidieh, A., Vinitsky, E., and Bayen, A., 2018. Flow: Deep reinforcement learning for control in sumo. *EPiC Series in Engineering*, 2:134–151.
- Kouvelas, A., Saeedmanesh, M., and Geroliminis, N., 2017. Enhancing model-based feedback perimeter control with data-driven online adaptive optimization. *Transp. Res. Part B: Methodol.*, 96:26–45.
- Leclercq, L., Chiabaut, N., and Trinquier, B., 2014. Macroscopic fundamental diagrams: A cross-comparison of estimation methods. *Transp. Res. Part B: Methodol.*, 62:1–12.
- Lei, T., Hou, Z., and Ren, Y., 2019. Data-driven model free adaptive perimeter control for multi-region urban traffic networks with route choice. *IEEE Trans. Intell. Transp. Syst.*
- Lewis, F. L., Vrabie, D., and Syrmos, V. L., 2012. *Optimal control*. John Wiley & Sons.
- Li, Y., Yildirimoglu, M., and Ramezani, M., 2021. Robust perimeter control with cordon queues and heterogeneous transfer flows. *Transp. Res. Part C*, 126:103043.
- Loder, A., Ambühl, L., Menendez, M., and Axhausen, K. W., 2019. Understanding traffic capacity of urban networks. *Scientific reports*, 9(1):1–10.
- Lopez, P. A., Behrisch, M., Bieker-Walz, L., Erdmann, J., Flötteröd, Y.-P., Hilbrich, R., Lücken, L., Rummel, J., Wagner, P., and Wießner, E., 2018. Microscopic traffic simulation using sumo. In *2018 21st international conference on intelligent transportation systems (ITSC)*, pages 2575–2582. IEEE.
- Lowrie, P., 1982. The sydney coordinated adaptive traffic (scat) system-principles, methodology, algorithm. In *Proc. of International Conference on Road Traffic Signaling*, pages 67–70. IEE.
- Lyashevskiy, S., 1996. Constrained optimization and control of nonlinear systems: new results in optimal control. In *Proceedings of 35th IEEE conference on decision and control*, volume 1, pages 541–546. IEEE.
- Lyshevski, S. E., 1998. Optimal control of nonlinear continuous-time systems: design of bounded controllers via generalized nonquadratic functionals. In *Proceedings of the 1998 American Control Conference. ACC (IEEE Cat. No. 98CH36207)*, volume 1, pages 205–209. IEEE.
- Mercader, P. and Haddad, J., 2021. Resilient multivariable perimeter control of urban road networks under cyberattacks. *Control Engineering Practice*, 109:104718.
- Mnih, V., Kavukcuoglu, K., Silver, D., Rusu, A. A., Veness, J., Bellemare, M. G., Graves, A., Riedmiller, M., Fidjeland, A. K., Ostrovski, G., et al., 2015. Human-level control through deep reinforcement learning. *Nature*, 518(7540):529.
- Modares, H., Lewis, F. L., and Naghibi-Sistani, M.-B., 2014. Integral reinforcement learning and experience replay for adaptive optimal control of partially-unknown constrained-input continuous-time systems. *Automatica*, 50:193–202.
- Papageorgiou, M., Diakaki, C., Dinopolou, V., Kotsialos, A., and Wang, Y., 2003. Review of road traffic control strategies. *Proceedings of the IEEE*, 91(12):2043–2067.
- Ramezani, M., Haddad, J., and Geroliminis, N., 2015. Dynamics of heterogeneity in urban networks: aggregated traffic modeling and hierarchical control. *Transp. Res. Part B: Methodol.*, 74:1–19.
- Ren, Y., Hou, Z., Sirmatel, I. I., and Geroliminis, N., 2020. Data driven model free adaptive iterative learning perimeter control for large-scale urban road networks. *Transp. Res. Part C*, 115:102618.
- Saeedmanesh, M. and Geroliminis, N., 2017. Dynamic clustering and propagation of congestion in heterogeneously congested urban traffic networks. *Transportation research procedia*, 23:962–979.
- Saeedmanesh, M., Kouvelas, A., and Geroliminis, N., 2021. An extended kalman filter approach for real-time state estimation in multi-region mfd urban networks. *Transp. Res. Part C*, 132:103384.
- Silver, D., Huang, A., Maddison, C. J., Guez, A., Sifre, L., Van Den Driessche, G., Schrittwieser, J., Antonoglou, I., Panneershelvam, V., Lanctot, M., et al., 2016. Mastering the game of go with deep neural networks and tree search. *Nature*, 529(7587):484.
- Sirmatel, I. I. and Geroliminis, N., 2019. Nonlinear moving horizon estimation for large-scale urban road networks. *IEEE Trans. Intell. Transp. Syst.*, 21(12):4983–4994.
- Sirmatel, I. I. and Geroliminis, N., 2021. Stabilization of city-scale road traffic networks via macroscopic fundamental diagram-based model predictive perimeter control. *Control Engineering Practice*, 109:104750.
- Sirmatel, I. I., Tsitsokas, D., Kouvelas, A., and Geroliminis, N., 2021. Modeling, estimation, and control in large-scale urban road networks with remaining travel distance dynamics. *Transp. Res. Part C*, 128:103157.
- Su, Z., Chow, A. H., Zheng, N., Huang, Y., Liang, E., and Zhong, R., 2020. Neuro-dynamic programming for optimal control of macroscopic fundamental diagram systems. *Transp. Res. Part C*, 116:102628.
- Sutton, R. S. and Barto, A. G., 2018. *Reinforcement learning: An introduction*. MIT press.
- Vrabie, D., Pastravanu, O., Abu-Khalaf, M., and Lewis, F., 2009. Adaptive optimal control for continuous-time linear systems based on policy iteration. *Automatica*, 45(2):477 – 484.
- Yildirimoglu, M. and Geroliminis, N., 2014. Approximating dynamic equilibrium conditions with macroscopic fundamental diagrams. *Transp. Res. Part B: Methodol.*, 70:186–200.

- Zhong, R., Chen, C., Huang, Y., Sumalee, A., Lam, W., and Xu, D., 2018a. Robust perimeter control for two urban regions with macroscopic fundamental diagrams: a control-lyapunov function approach. *Transp. Res. Part B: Methodol.*, 117:687–707.
- Zhong, R., Huang, Y., Chen, C., Lam, W., Xu, D., and Sumalee, A., 2018b. Boundary conditions and behavior of the macroscopic fundamental diagram based network traffic dynamics: A control systems perspective. *Transp. Res. Part B: Methodol.*, 111:327 – 355.
- Zhong, R. X., Sumalee, A., Pan, T. L., and Lam, W. H., 2014. Optimal and robust strategies for freeway traffic management under demand and supply uncertainties: an overview and general theory. *Transportmetrica A: Transport Science*, 10(10):849–877.
- Zhou, D. and Gayah, V. V., 2021. Model-free perimeter metering control for two-region urban networks using deep reinforcement learning. *Transp. Res. Part C*, 124:102949.
- Zhou, Z., De Schutter, B., Lin, S., and Xi, Y., 2016. Two-level hierarchical model-based predictive control for large-scale urban traffic networks. *IEEE Transactions on Control Systems Technology*, 25(2):496–508.